# Occurrence of Differences between Alkali and Alkaline Earth Metals (AAEMs), Including Sodium, Potassium, Calcium, and Magnesium, in the Maceral Groups of the Xiheishan Coal, Zhundong Coalfield, Xinjiang, China

Kexin Che [1,2], Jiaxin Li [3], Qingfeng Lu [1,2], Fengjun Shao [1,2,3], Wenlong Wang [1,2], Wenfeng Wang [1,2,3,*] and Xin He [4,*]

1. Key Laboratory of Coalbed Methane Resources and Reservoir Formation Process, Ministry of Education, China University of Mining and Technology, Xuzhou 221008, China; 17851143107@163.com (K.C.); luqingfeng@cumt.edu.cn (Q.L.); sfj_leap@163.com (F.S.); tb21010023b4@cumt.edu.cn (W.W.)
2. School of Resources and Geosciences, China University of Mining and Technology, Xuzhou 221116, China
3. School of Geology and Mining Engineering, Xinjiang University, Urumqi 830047, China; ljiaxin0306@163.com
4. Key Laboratory of Coal Processing & Efficient Utilization, Ministry of Education, School of Chemical Engineering and Technology, China University of Mining & Technology, Xuzhou 221116, China
* Correspondence: wangwenfeng@cumt.edu.cn (W.W.); hexin_kd@126.com (X.H.); Tel.: +86-1377588117 (W.W.); +86-19851629820 (X.H.)

**Abstract:** This study investigated the differences and correlation between the occurrence characteristics of alkali and alkaline earth metals (AAEMs) among different maceral groups in high-alkali, high-inertinite coal, and provides scientific guidance for the co-separation of AAEMs and inertinite groups in Xinjiang coal. The total AAEMs of inertinite-enriched samples were significantly higher than those in raw coals and vitrinite-enriched samples. Five-step sequential extraction showed that Na mainly occurs as water-soluble sodium (Na-Water) in raw coal and inertinite-enriched samples, accounting for about 53% of the total content, while it exists as organic sodium (Na-NH$_4$Cl and Na-EDTA) in vitrinite-enriched samples, accounting for about 52% of the total content. Ca and Mg are both mainly present in organic form (Ca/Mg-NH$_4$Cl and Ca/Mg-EDTA) in all the samples, with slightly higher proportions present in vitrinite-enriched samples. The contents of K are low in all the samples, which exist in an insoluble state (K-I). Combined microscopy and SEM-EDS analyses have revealed that the localized enrichment of Na in raw coal and inertinite-enriched samples occurs in the inertinite cell cavity, which primarily exists as NaHCO$_3$ combined with quartz crystals, with a maximum content of up to 5.85 wt%. In this study, although EDS spectra could not directly characterize organic Ca and Mg, dolomite and calcite minerals were repeatedly found in the inertinite cell cavity. Moreover, the contents of Ca and Mg in the vitrinite-enriched samples were significantly lower than those in the other samples, which suggests that Ca and Mg are enriched with the inertinite groups. The localized enrichment of AAEMs could not be detected in any of the vitrinite-enriched samples. In summary, though there are significant differences between the occurrence modes of AAEMs in different maceral groups of high-alkali coal, AAEMs have a strong affinity with inertinite, which may be due to the inertinite's abundant pore structures.

**Keywords:** high-inertinite high-alkali coal; alkali and alkaline earth metals (AAEMs); occurrence modes; maceral group

## 1. Introduction

Xinjiang is one of the dominant strategic implementation areas for the clean and efficient utilization of coal in China, with the coal reserves of Zhundong coalfield totaling $3.9 \times 10^{11}$ t, accounting for 17.8% of Xinjiang's overall coal reserves. Zhundong coalfield is a vital coal production base, as it ensures a stable supply of coal energy in China [1,2].

Coal extracted from the Zhundong coalfield is characterized by its low sulfur contents, low ash production, medium and high calorific value, and low contents of harmful elements, making it an ideal raw material for power generation and use in the coal chemical industry [3,4]. However, the unique coal-forming environment and the high levels of groundwater salinization have led to the presence of high contents of alkali and alkaline earth metals (AAEMs) in coal from Xinjiang's Zhundong coalfield. Due to the low melting points of AAEMs, slagging and fouling are serious issues in high-alkali coal during the combustion process, which significantly limits its use in power station boilers [5–7]. In general, AAEMs in coal mainly exist in either inorganic or organic form [8]. The different occurrence modes in coal determine the roles of AAEMs in coal transformation. Many studies have shown that water-soluble AAEMs have intense volatility, which is the leading cause of equipment corrosion [9,10]. AAEMs, when combined with organic matter, can promote coal combustion and gasification to some extent [11–13], but they can also be volatile and damage equipment [14], meaning that the harm is lower than that caused by water-soluble AAEMs. Insoluble AAEMs with high thermal stability struggle to decompose and become volatile, making them the least hazardous option [15]. Consequently, clarifying the occurrence mode of AAEMs in Zhundong coal can provide theoretical support for developing corresponding AAEMs removal methods so as to effectively avoid the problem of equipment ash and slag accumulation during coal burning.

Meanwhile, Zhundong coal is characterized by a high content of inertinite group macerals, which have extremely high contents of fusinite and semi-fusinite, reaching 40%~70% [16], much higher than the general 10%~20% levels of bituminous coal found in other parts of China [8]. Zhao et al. [17] studied the pyrolysis of the vitrinite and inertinite groups of coal, showing that the inertinite group had low pyrolysis reactivity, low tar and gas yields, and a high water yield compared to vitrinite. The high-carbon and low-hydrogen contents of inertinite in coal seriously affect pyrolysis, liquefaction activity, and tar yield, hindering the efficient utilization of Zhundong coal [18]. In view of this, the simultaneous fulfilment of AAEMs removal and maceral separation is greatly significant for the clean and efficient utilization of Zhundong coal, which can not only effectively avoid equipment corrosion and other safety risks caused by AAEMs but also improve the utilization rate and conversion rate of Zhundong coal. However, most research has focused on the occurrence of AAEMs in Zhundong coal, and there is a lack of research on the differences in the occurrence of AAEMs between different maceral groups (vitrinite and inertinite) as well as their relationship. This makes it difficult to accurately remove AAEMs from coal while separating maceral groups.
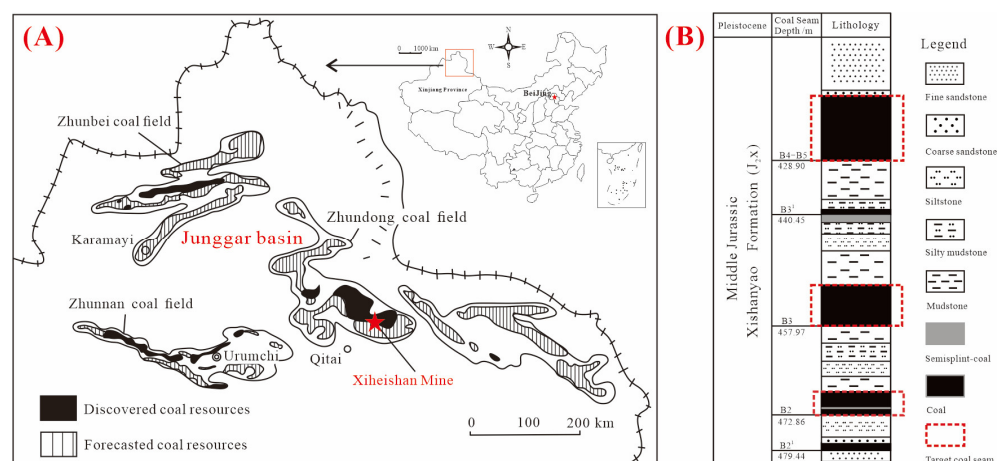
To this end, we extracted raw coal samples with different coal petrology characteristics from the Xiheishan Mine Zhundong coalfield in Xinjiang and manually extracted maceral concentrate samples to study the differences in occurrence and relationships between AAEMs in the maceral groups of Zhundong coal. The objectives of this study were as follows: (1) to clarify the distribution differences between AAEM contents in different maceral groups; (2) to classify and quantify the occurrence modes of AAEMs by using a new five-step sequential extraction method and investigate the differences between AAEMs in different maceral groups; (3) to observe the specific occurrence modes of AAEMs in the samples and reveal their potential relationships with macerals by combining microscopy and SEM-EDS analyses.

## 2. Geological Setting

The Zhundong coalfield in the Junggar Basin is located in Jimsar County, Changji Hui Autonomous Prefecture, Xinjiang Province, Northwest China. The main coal-bearing strata in the Zhundong coalfield are the Lower Jurassic Badaowan Formation ($J_1b$), the Lower Jurassic Sangonghe Formation ($J_1s$), the Middle Jurassic Xishanyao Formation ($J_2x$), and the Lower–Middle Jurassic Shishugou Group ($J_{2-3}sh^1$), of which the coal seam of the Middle Jurassic Xishanyao Formation ($J_2x$) is thick and the Lower Jurassic Badaowan Formation

($J_1b$), Lower Jurassic Sangonghe Formation ($J_1s$), and Lower–Middle Jurassic Shishugou Group ($J_{2-3}sh^1$) are thin and extremely unstable [19,20].

The Xiheishan Mine, situated in the southeastern part of the Zhundong coalfield within the study area, is characterized by its coal-bearing strata, such as the Xishanyao Formation ($J_2x$), which comprises a diverse range of fluvial facies, delta facies, swamp facies, and shallow lake facies deposits consisting of fine-coarse sandstone, siltstone, mudstone, and coal seams [20]. Figure 1 shows the sampling locations and their corresponding stratigraphic columns, and the labeled sampled coal seams are shown in Figure 1(B).



**Figure 1.** Location and representative stratigraphic column of Xiheishan Mining District: (**A**) distribution of the main coalfields and locations of sampling sites in Xinjiang Provence (★: sampling site locations; □: location of Junggar Basin); (**B**) stratigraphic column of coal-bearing stratum in Xiheishan Mine.

## 3. Experimental Section

### 3.1. Sample Preparation

During this investigation, we collected three raw samples from the B2, B3, and B5 coal seams of Xiheishan Mine in Zhundong coalfield. Vitrain was selected as the macrolithotype abundant in vitrinite. Vitrain strips with thickness between 3 and 10 mm were selected from the massive raw coal samples, the vitrain strips were gently removed with a small hammer and slice blades, and then the dull components on the samples surface were gently scraped off with slice blades and were used as the preliminary concentrates of the vitrinite group. Then, the primary vitrinite concentrates were crushed using an agate mortar and pestle until the particle size was approximately 1~3 mm. Subsequently, small particles exhibiting a deep black color, strong luster, and no mixture with other components were selected as the vitrinite concentrates using small tweezers. Fusain was selected as the macrolithotype abundant in inertinite. Firstly, the fusain layers with thickness of about 1~3 mm were selected from massive raw coal samples, and then they were gently scraped off with slice blades as the preliminary concentrates of the inertinite group. Then, the sharp end of the tweezers was used to slightly crush the scraped fusain flakes (thickness of about 1 mm), and the tweezers were used to select the particles with typical charcoal appearance and no other impurities as the inertinite concentrates. The separation operation used was also described in detail in our team's previous study [21]. Liptinite was excluded from this investigation due to its severe scarcity (<3%) in Zhundong coal [22–25]. Due to the differences between the macro-lithotype characteristics of different raw coals, vitrain and fusain cannot easily be found in all raw coals. In this study, vitrain and fusain were both collected in the B5 raw coal (B5-R), while only fusain was collected in the B2 raw coal (B2-R), and only vitrain was collected in the B3 raw coal (B3-R). The collected maceral concentrates were named B2-I, B3-V, B5-I, and B5-V. Three raw coal samples and four maceral concentrates samples were dried and crushed to below 0.88~0.38 mm and 0.074 mm, awaiting subsequent experimental use.

### 3.2. Sequential Extraction

A sequential extraction experiment is the most common type of method used to quantitatively investigate the occurrence states of AAEMs in coal [26]. Four-step sequential extraction using deionized water, ammonium acetate ($NH_4OAc$), hydrochloric acid (HCl), and digestive acid (HF, $HNO_3$, and $H_2O_2$) is the traditionally used experimental method. The extracted AAEMs can be defined as water-soluble (AAEMs-WS), exchangeable-soluble (AAEMs-AS), acid-soluble (AAEMs-HS), or insoluble (AAEMs-IS). However, the traditional method has many drawbacks, such as using a neutral ammonium acetate solution to dissolve some carbonate minerals ($CaCO_3$ and $MgCO_3$) in advance, meaning that some mineral forms of calcium and magnesium are mistaken for ion-exchange forms [26,27]. In addition, some Na, when combined with organic matter, becomes insoluble in ammonium acetate solution and might be extracted using hydrochloric acid [28,29]. The above circumstances cause inaccurate classification results.

To solve these problems, we proposed a new five-step sequential extraction process, using deionized water, 0.1 mol/L of $NH_4Cl$ solution (buffered to pH = 8.5 with $NH_3 \cdot H_2O$), 0.1 mol/L of $NH_4$-EDTA solution (buffered to pH = 9 with $NH_3 \cdot H_2O$), 1 mol/L of HCl, and digestive acids (HF, $HNO_3$, and $H_2O_2$) as the extraction solution, as it can obtain water-soluble AAEMs (AAEMs-Water), AAEMs bound to carboxyl groups (AAEMs-$NH_4Cl$), AAEMs in the form of chelates or AAEMs combined with functional groups other than carboxyl groups (AAEMs-EDTA), acid-soluble carbonate-bound AAEMs (AAEMs-HCl), and insoluble AAEMs (AAEMs-I). This process was described in detail in our previous study, and some progress has since been made [21,28]. In this study, we compared the traditional four-step extraction process to the improved five-step extraction process. The specific process and related parameters are shown in Figure 2.
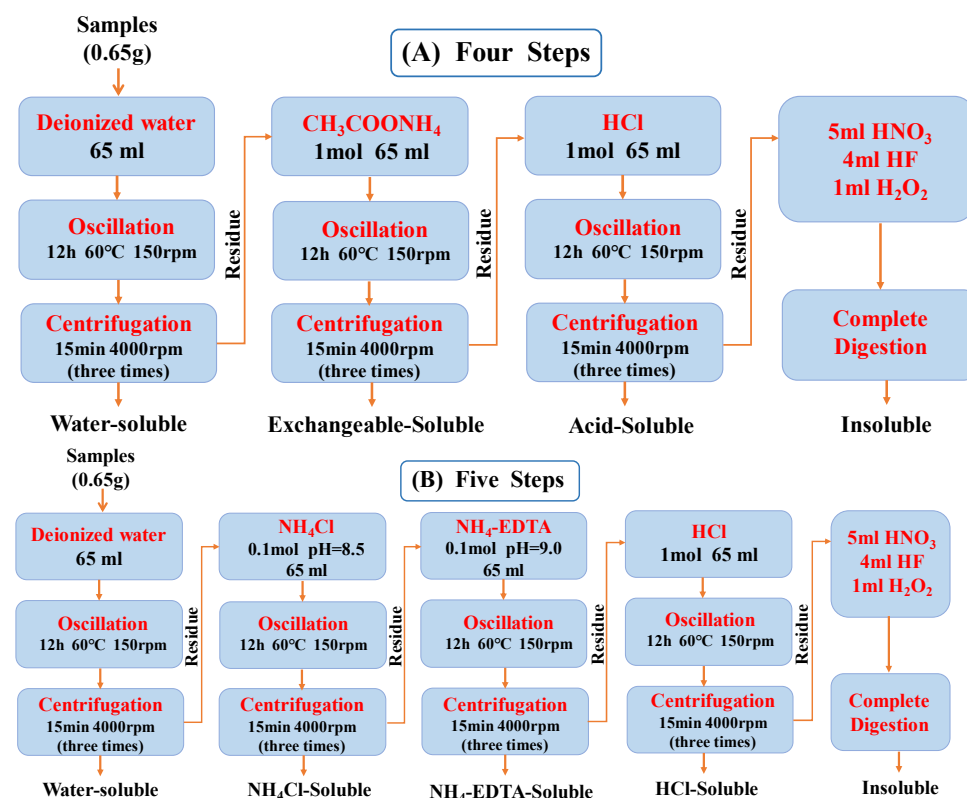


**Figure 2.** The flow diagram of the four-step and five-step sequential extraction procedure.

The contents of $Na^+$, $Mg^{2+}$, $K^+$, and $Ca^{2+}$ in filtrate after extraction and final residue digestion solution were determined using an inductively coupled plasma atomic emission

spectrometer (ICP-AES, Thermo Fisher Company, Waltham, MA, USA). Each group was tested twice to ensure the accuracy of the experimental data.

### 3.3. Analytical Methods

The sample's moisture, ash, volatile matter yield, and fixed carbon contents were determined and calculated using the Chinese national standard "Proximate Analyses of Coal (GB/T 212-2008 [30])".

According to the "Determination of total sulfur in coal (GB/T 214-2007 [31])", the Eschka method of determination was used for determining the total contents of sulfur in samples. The samples' C, H, and N contents were determined according to the Chinese national standards GB/T 19227-2008 [32] and GB/T 476-2008 [33], and the O content was calculated.

Using an epoxy resin curing agent, the sample with a particle size of 0.88~0.38 mm was prepared through deconstruction into pulverized coal bricks and diamond polishing fluid was used for polishing. Based on the ICCP System 1994 [34–37], the maceral composition of seven samples was identified and photographed using fluorescence optical microscopy (Imager M1 m, Carl Zeiss, Jena, Germany), and the liptinite was identified using fluorescence light attachment. According to the Chinese national standard GB/T 6948-2008 [38], the random reflectance of vitrinite was determined by microphotometer (MV-SP, Leica, Wetzlar, Germany), with sapphire as the standard samples. A scanning electron microscope (SIGMA, Carl Zeiss, Oberkochen, Germany), coupled with energy-dispersive X-ray spectroscopy (EDS) and observation and element testing of AAEM particles in coal via point and regional surface scanning, was also used.

The contents of trace elements in raw coal were measured via inductively coupled plasma mass spectrometry (ICP-MS, Thermo Elemental X-II). The $Cl^-$, $SO_4^{2-}$, and $NO_3^-$ concentrations in the solution were detected using an ion chromatograph (IC, type 883 of Wantone, Switzerland). The concentrations of $CO_3^{2-}$ and $HCO_3^-$ in the detection solution were determined according to DZ/T 0064.49-2021 "Methods for analysis of groundwater water quality-Part 49: Determination of carbonate, bicarbonate and hydroxide ions titration method".

## 4. Results and Discussion
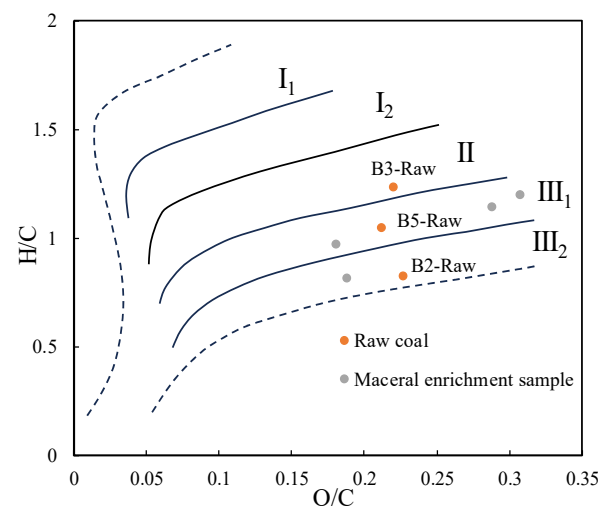
### 4.1. Assessment of Coal Quality

The results of the determination of the total sulfur contents, proximate and ultimate analyses, and vitrinite random reflectance values test of the seven samples are shown in Table 1. All samples are of ultra-low-sulfur and low-sulfur coal (0.33%–0.53%). In the proximate analyses, the ash contents of all the samples are low, as they constitute ultra-low-ash coal (2.52%–3.58%). Differently, B2-R, B5-R, and the inertinite-enriched samples contain more moisture (>15.61%) and fixed carbon (>63.22%) than B3-R and the vitrinite-enriched samples. The high moisture content of the inertinite-enriched samples may be attributed to their richer pore structure and higher concentration of hydrophilic groups [39,40]. B3-R and the vitrinite-enriched samples exhibit a higher volatile matter content (>41.04%) compared to B2-R, B3-R, and the inertinite-enriched samples. According to the vitrinite random reflectance values, B3-R, B2-R, and B5-R are all low-rank coals.

According to the ultimate analysis results, the inertinite-enriched samples exhibit higher carbon levels compared to those of the corresponding raw coals, while the vitrinite-enriched samples demonstrate an opposite trend. In addition, there was no significant variation in the hydrogen content between all the samples. The Van Krevelen chart [41] is a two-dimensional model diagram that shows the evolution of organic matter in coal, and is usually used to classify the kerogen type and determine the type of hydrocarbon source rocks [42]. According to Figure 3, the kerogen types of the three raw coals are also different. The kerogen type of B2-R constitutes $III_2$, the kerogen type of B5-R constitutes $III_1$, and the kerogen type of B3-R constitutes II. B3-R has a greater hydrocarbon generation capacity than the other raw coals.

**Table 1.** Proximate analyses, ultimate analyses, and vitrinite reflectance results of samples.

| Samples | Proximate Analyses (w%) | | | | Ultimate Analyses (wad%) | | | | | VR | H/C | O/C |
|---|---|---|---|---|---|---|---|---|---|---|---|---|
| | Mad | Ad | Vdaf | FCd | Cdaf | Hdaf | Odaf | Ndaf | St,d | | | |
| B2-R | 18.98 | 3.58 | 29.92 | 63.22 | 72.14 | 4.94 | 21.83 | 0.57 | 0.53 | 0.49 | 0.82 | 0.23 |
| B2-I | 17.17 | 2.54 | 28.56 | 64.62 | 75.1 | 5.08 | 18.89 | 0.53 | 0.40 | 0.51 | 0.81 | 0.19 |
| B3-R | 13.83 | 3.76 | 41.04 | 55.37 | 70.42 | 7.24 | 20.71 | 1.09 | 0.54 | 0.41 | 1.23 | 0.22 |
| B3-V | 10.76 | 3.25 | 46.60 | 50.63 | 66.73 | 6.34 | 25.63 | 0.83 | 0.48 | 0.38 | 1.14 | 0.29 |
| B5-R | 15.61 | 3.29 | 32.02 | 65.74 | 72.27 | 6.29 | 20.44 | 0.68 | 0.33 | 0.44 | 1.04 | 0.21 |
| B5-I | 17.12 | 2.63 | 28.91 | 64.22 | 74.95 | 6.05 | 18.07 | 0.55 | 0.38 | 0.48 | 0.97 | 0.18 |
| B5-V | 11.09 | 2.52 | 45.29 | 52.28 | 65.97 | 6.58 | 27.09 | 0.54 | 0.41 | 0.40 | 1.20 | 0.31 |

ad: air-dried basis; d: dry basis; daf: dry and ash-free basis; M: moisture; A: ash yield; V: volatile matter; FC: fixed carbon; VR: vitrinite reflectance.



**Figure 3.** Van Krevelen chart of coal samples.

The contents of critical metal elements in raw seam coals compared to those of the Chinese and worldwide coals [43] are presented in Table 2. Overall, the majority of critical metal element contents in the three raw coals are extremely low, being significantly below the world average level for all coals, except for Sr. The relative enrichment of Sr may be due to the adsorption of free Sr by coal seams during the replenishment of groundwater by salinized surface water [44].

**Table 2.** Critical metal elements and rare earth elements in raw coals (μg/g).

| Raw Coal | Li | Be | Sc | V | Cr | Co | Ga | Rb | Sr |
|---|---|---|---|---|---|---|---|---|---|
| B2-R | 11.00 | 0.04 | 0.16 | 0.98 | 2.08 | 0.54 | 0.14 | 0.37 | 215.00 |
| B3-R | 9.06 | 0.07 | 0.93 | 8.59 | 8.55 | 8.89 | 0.63 | 0.26 | 153.00 |
| B5-R | 5.53 | 0.03 | 0.18 | 0.61 | 0.94 | 0.36 | 0.17 | 0.20 | 181.00 |
| China [39] | 31.80 | 2.11 | 4.38 | 35.10 | 15.40 | 7.08 | 6.55 | 9.25 | 140.00 |
| World [39] | 12.00 | 2.00 | 3.90 | 25.00 | 16.00 | 5.10 | 5.80 | 14.00 | 110.00 |
| **Raw coal** | **Nb** | **Mo** | **Cd** | **In** | **Cs** | **Ta** | **W** | **U** | **∑REY** |
| B2-R | 0.60 | 0.07 | 0.02 | 0.002 | 0.07 | 0.01 | 0.004 | 0.05 | 3.90 |
| B3-R | 1.64 | 0.87 | 0.01 | 0.006 | 0.03 | 0.06 | 0.140 | 0.18 | 11.70 |
| B5-R | 0.60 | 0.08 | 0.01 | 0.001 | 0.03 | 0.02 | 0.032 | 0.06 | 4.20 |
| China [39] | 22.30 | 3.08 | 0.25 | 0.05 | 1.13 | 0.62 | 1.08 | 2.43 | 137.90 |
| World [39] | 12.00 | 2.20 | 0.22 | 0.03 | 1.00 | 0.28 | 1.10 | 2.40 | 68.50 |

### 4.2. Maceral Compositions of the Samples

The maceral composition for the seven samples is shown in Table 3. The proportion of inertinite in the B2-R is 73.6%, which constitutes a typical inertinite-rich coal present in the
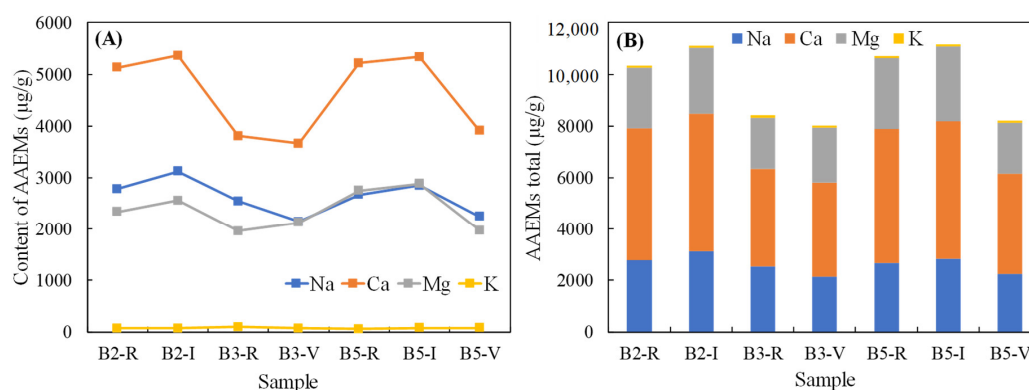
Zhundong coalfield. The proportion of vitrinite is slightly lower than that of inertinite in the B5-R, having proportions of 41.9% and 57.9%, respectively. The B3-R is a rich vitrinite group coal with a vitrinite group content of 70.8%. For the manually separated, maceral concentrates, the contents of vitrinite in the vitrinite-enriched samples B3-V and B5-V are higher than 90%, and the contents of inertinite in the inertinite-enriched samples B2-I and B5-I are higher than 80%. Four extracted maceral concentrates were adequately represented, with purities exceeding 80%. The purity of the extracted maceral enrichments exceeds 80%.

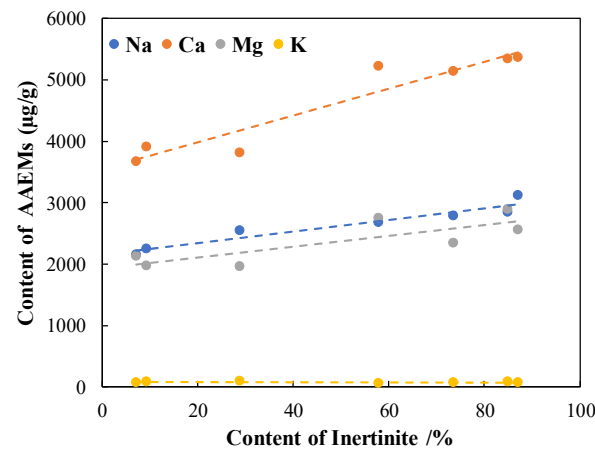**Table 3.** Identification of macerals in coal samples.

| Sample | Mineral Matter Free Basis (vol)/% | | |
|---|---|---|---|
| | Vitrinite | Inertinite | Liptinite |
| B2-R | 26.2 | 73.6 | 0.2 |
| B2-I | 12.5 | 87.1 | 0.4 |
| B3-R | 70.8 | 28.8 | 0.4 |
| B3-V | 92.4 | 7.2 | 0.4 |
| B5-R | 41.9 | 57.9 | 0.2 |
| B5-I | 14.7 | 84.9 | 0.4 |
| B5-V | 90.2 | 9.4 | 0.4 |

*4.3. Contents of the AAEMs in the Samples*

Figure 4 shows the contents of Na, Mg, K, and Ca and the total contents of AAEMs in the seven samples. As shown in Figure 4A, the AAEMs in Xiheishan coal are mainly Na, Mg, and Ca, and the content of K is minimal. The distribution patterns of Na, Mg, and Ca were similar, with the concentrations of these elements in samples with high vitrinite contents (B3-R, B3-V, and B5-V) being comparatively lower than those in the other samples. The coal formation period of Zhundong coalfield was not significantly influenced by sediment sources or seawater; the AAEMs in coal mainly originate from the infiltration of AAEM ions from the highly salinized epipedon and overlying strata into the coal seam with groundwater [44,45]. In addition, Figure 4B shows that the total AAEM contents in inertinite-enriched samples (B2-I, B5-I) were significantly higher than those in raw coal and vitrinite-enriched samples. The inertinite-enriched sample B5-I had the highest total amount of AAEMs (11,145.70 µg/g), while the vitrinite-enriched sample B3-V had the lowest total amount (8010.11 µg/g). Figure 5 shows the cross-plot of the inertinite and AAEM contents of the samples. With the increase in the inertinite content, the contents of Na, Ca, and Mg displayed a significant upward trend. In summary, the contents of AAEMs in coal were different in different maceral components, and there was a tendency for AAEMs to be enriched in the inertinite-enriched samples.
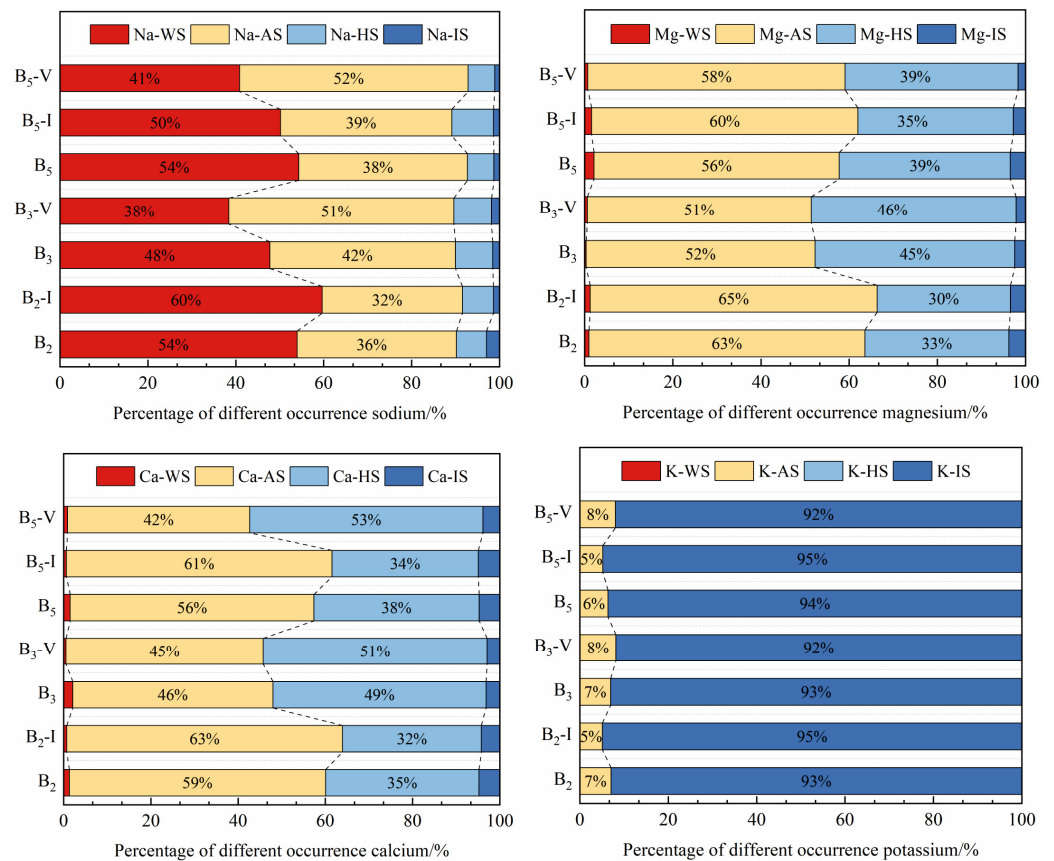


**Figure 4.** Content of AAEMs in samples. (**A**) Content of Na, Ca, Mg and K in samples, respectively (**B**) Total AAEM content in samples.

**Figure 5.** The cross-plot of inertinite and AAEMs content of the samples.

### 4.4. Sequential Extraction Results for the AAEMs

Figures 6 and 7 show the quantitative analysis results of the AAEM contents in each occurrence mode, as obtained via the four-step sequential extraction and the five-step sequential extraction methods, respectively. This section will compare the two extraction methods to analyze the occurrence modes of Na, Mg, Ca, and K in the samples.



**Figure 6.** Experimental results of four-step sequential extraction.

**Figure 7.** Experimental results of five-step sequential extraction.

Regarding the occurrence mode of Na in coal, the results of the four-step sequential extraction and five-step sequential extraction methods are similar. The five-step sequential extraction method divides sodium present in organic form into Na-NH$_4$Cl and Na-EDTA, which are more detailed sub-categories; the results of the five-step sequential extraction method will now be discussed.

In the raw coal (B2-R, B3-R, B5-R) and inertinite-enriched samples (B2-I, B5-I), Na mainly exists in the form of water-soluble Na (Na-Water), with an average proportion of 53.24%. The relative contents were ranked as follows: B2-I > B5-I > B2 > B5 > B3. As can be seen, the proportions of Na-Water in the inertinite-enriched samples were higher than those in the raw coal samples, and the proportion of Na-Water in the B3-R with low inertinite content was relatively low. In contrast, Na in the vitrinite-enriched sample (B3-V, B5-V) mainly existed in the form of organic sodium (Na-NH$_4$Cl and Na-EDTA), and it had an average proportion of 52.48%, of which Na-NH$_4$Cl was significantly higher than Na-EDTA, indicating that, in Xiheishan coal, organic sodium is mainly combined with carboxyl groups in coal to form organic complexes. This difference was present because Na-Water in coal mainly originates from the enrichment of high-alkaline water in coal-forming swamps and the infiltration of highly mineralized groundwater into coal seams after the sedimentary period [45]. Furthermore, the inertinite of coal has a more abundant pore structure, which makes it easier to enrich Na-Water in coal [28]. Meanwhile, the vitrinite-enriched samples (B3-V and B5-V) were less metamorphic and had more abundant oxygenated functional groups (organic acids) [46], which made it easier to form organic sodium with Na$^+$. Finally, the Na-HCl (average percentage: 6.43%) and Na-I (average percentage: 2.12%) contents in each of the seven samples were so low that there were no significant differences between each sample; these results will not be recounted.

According to the results of the four-step sequential extraction methods, Ca contents in coal mainly exist in the form of Ca-AS and Ca-HS, with high Ca-AS content percentages

present in B2-R, B5-R, B2-I, and B5-I and high Ca-HS content percentages present in B3-R, B3-V, and B5-V. However, in the results of the five-step sequential extraction methods, Ca-EDTA was the main occurrence mode of Ca in coal, followed by Ca-HCl and Ca-NH$_4$Cl. This shows that Ca in Xiheishan coal does not mainly exist in the form of calcium carboxylate but as chelates or in combination with functional groups other than carboxylic groups.

The four-step sequential extraction method also led to the inaccurate classification of the occurrence mode of Mg. Therefore, the results of the five-step extraction method are analyzed below. As shown in Figure 6, the occurrence modes of Mg and Ca in coal are relatively similar, both of which being mainly combined with organic matter. The relative contents of each occurrence mode are sorted as follows: Mg-EDTA $\approx$ Mg-NH$_4$Cl > Mg-HCl > Mg-I > Mg-Water.

The main form of K present in Xiheishan coal is insoluble K (K-I), with an average proportion of 93.9% (Figures 6 and 7). Our results also show that the main form of K present in Xiheishan coal is inorganic potassium, and it exists in the form of aluminosilicate. In contrast to the other AAEM contents in Xiheishan coal, the K content is relatively low, and the aluminosilicate minerals are not volatile at high temperatures, reducing the influence of boiler slagging.

### 4.5. The Form in which Water-Soluble AAEMs Exist

The concentrations of anions in the sample's water filtration solution are shown in Table 4. Considering the lower proportions of water-soluble Ca and Mg and the absence of water-soluble K in Xiheishan coal, the form in which water-soluble Na exists was carefully analyzed. Table 4 shows that the anions that are soluble in water in Xiheishan coal are mainly HCO$_3^-$ and SO$_4^{2-}$, as well as a small amount of Cl$^-$ ions, while NO$_3^-$ and CO$_3^{2-}$ have not been detected. This shows that the water-soluble Na in Xiheishan coal mainly exists in the form of NaHCO$_3$, Na$_2$SO$_4$, NaCl, or hydrated ions. The concentrations of HCO$_3^-$ in the vitrinite-enriched samples B3-V and B5-V are lower than those in the other samples, which further verifies the sequential extraction result stating that the proportion of water-soluble sodium in the vitrinite-enriched samples is relatively low.

**Table 4.** Anion concentration in water-soluble filtrate.

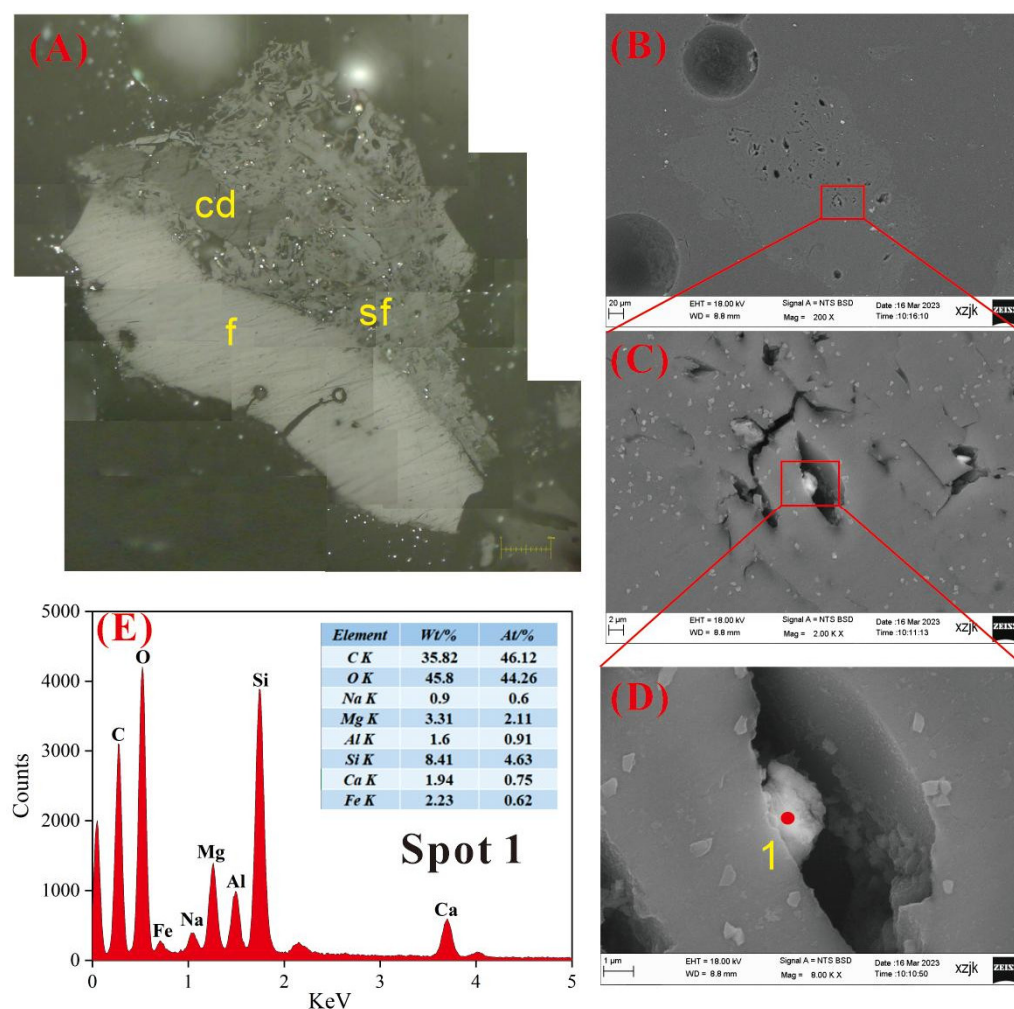| Sample | Anion Concentration/(mg/L) | | | | |
|---|---|---|---|---|---|
| | Cl$^-$ | SO$_4^{2-}$ | NO$_3^-$ | CO$_3^{2-}$ | HCO$_3$ |
| B2-R | 0.21 | 1.48 | - | - | 18.12 |
| B2-I | 0.15 | 1.12 | - | - | 20.45 |
| B3-R | 0.12 | 1.86 | - | - | 12.21 |
| B3-V | - | 0.85 | - | - | 7.66 |
| B5-R | 0.16 | 2.74 | - | - | 16.57 |
| B5-I | 0.18 | 1.06 | - | - | 19.15 |
| B5-V | 0.03 | 1.23 | - | - | 8.78 |

Note: - indicates that the ion is not detected.

### 4.6. Occurrence Characteristics of the AAEMs in Macerals

In this section, we study the differences between the occurrence statuses of AAEMs in different macerals and further clarify the relationship between AAEMs and macerals. Firstly, SEM-EDS tests were performed on all samples, and a comprehensive point and area analysis of the samples was performed to detect AAEMs-containing particles and position-label them. Then, the maceral compositions of AAEMs-containing particles were observed by optical microscopy under reflected light and oil immersion. It is worth noting that the samples needed to be ground and polished again prior to observation via optical microscopy, which may have led to differences in the morphologies of the particles observed via microscopy and SEM-EDS.

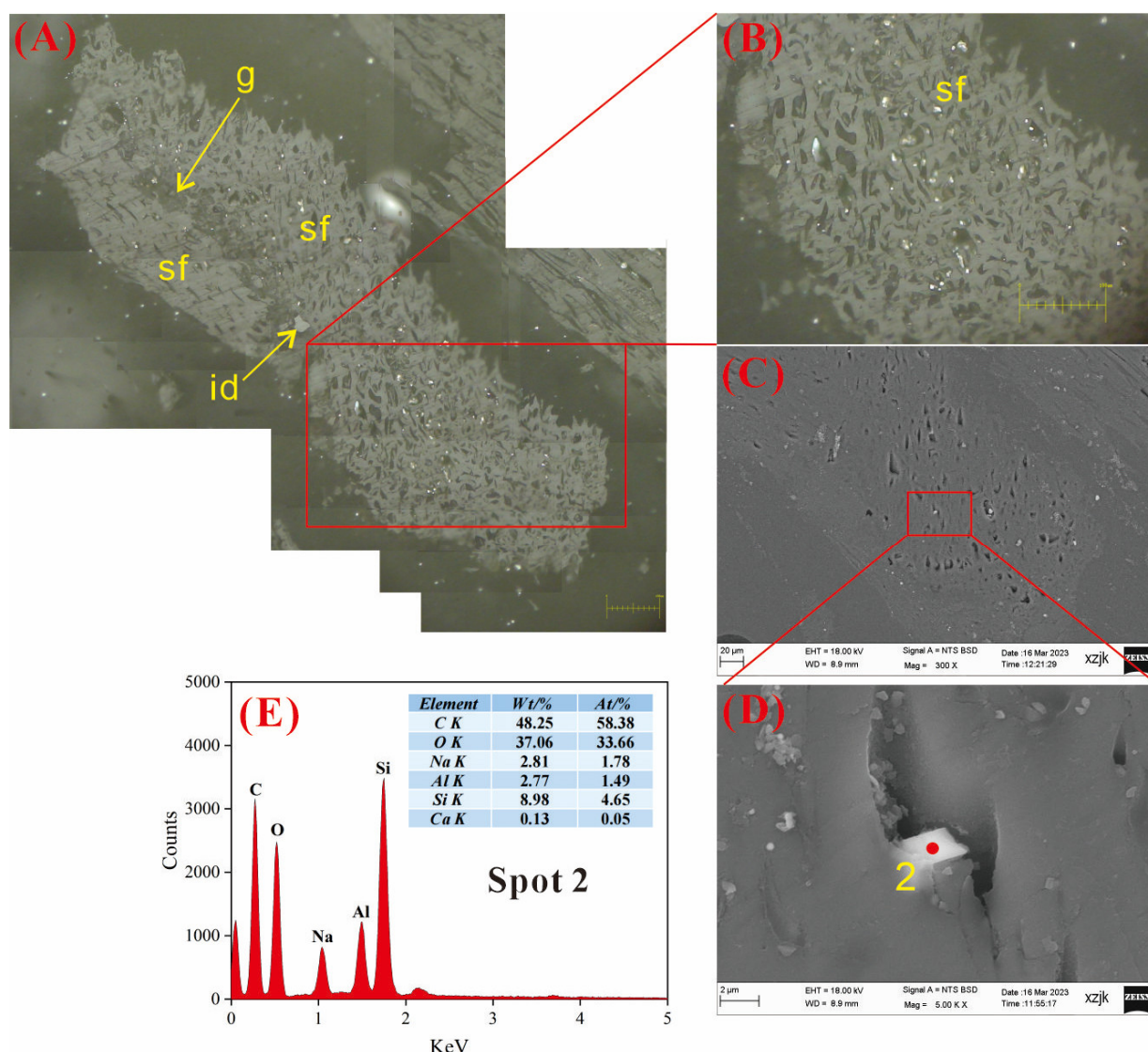### 4.6.1. AAEMs Occurrence Characteristics of B2-R and B2-I

The observations of B2-I are shown in Figures 8–10, respectively. Figure 8 shows an AAEMs-containing particle found in B2-I, which is a grain mainly composed of fusinite and semifusinite. One of the cells had irregularly shaped white crystals. Based on the results of the EDS spectrum (Figure 8E), a certain level of enrichment in AAEMs was detected at Spot 1 on the mineral crystal, with Al, Si, Ca, Mg, and Na present at this location. Notably, Mg exhibited slight enrichment (3.31 wt%). The Si/Al atomic ratio at this spot is 5.1, which rules out the possibility of kaolinite, suggesting that it is a magnesium-rich montmorillonite–chlorite mixed-layer clay mineral, where AAEMs exist in the form of mineral binding in the clay mineral.



**Figure 8.** Microscope and SEM–EDS identification of B2-I: (**A**) a particle composed of fusinite (f) and semifusinite (sf) adorned by a long ribbon-shaped collodetrinite (cd) on edge; (**B**) SEM image of (**A**); (**C**) magnified SEM image of the red boxed area in (**B**); (**D**) enlarged SEM image of sodium-containing mineral particles; (**E**) EDS spectra from Spot 1.

Figure 9 is also a semifusinite (sf) particle observed in B2-I, in which gellinite (g) serves as a binding agent for semifusinite and inertodetrinite (id) appears as an irregular particle in gellinite. A plate-like crystal was observed within a cellular cavity in semifusinite (Figure 9D), and the results obtained via EDS analysis reveal an atomic ratio for Na, Al, and Si of approximately 1:1:3 (Figure 9E). This indicates that the crystal could be identified as albite ($NaAlSi_3O_8$), which is recognized as a typical alkaline feldspar. In addition, trace

amounts of Ca were detected, which displace Na in the crystal lattice of albite in the form of isomorphism.
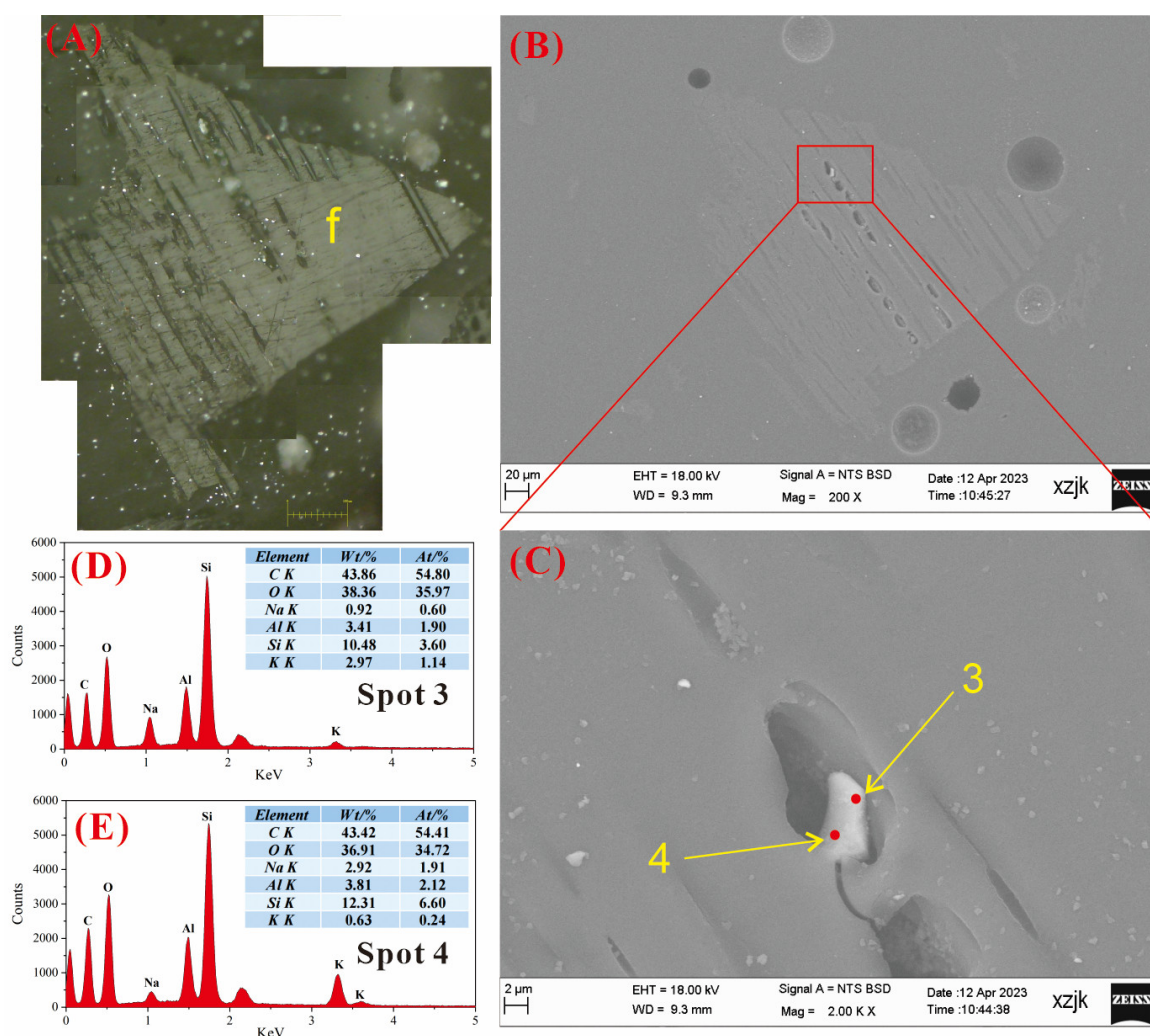


**Figure 9.** Microscope and SEM–EDS identification of B2-I: (**A**) a semifusinite (sf) particle, gellinite (g) serving as a binding agent for semifusinite (sf); (**B**) magnified microscope image of the red boxed area in (**A**); (**C**) SEM image of (**B**); (**D**) magnified SEM image of the red boxed area in (**C**); (**E**) EDS spectra from Spot 2.

Figure 10 shows the presence of alkaline feldspar minerals within the cellular cavity of a fusinite particle identified in B2-I. It can be seen from the EDS spectra results shown in Figure 8D that the AAEMs-containing crystal is a potassium feldspar–albite blend, and it has a high K content (2.97 wt%) in the crystal center and a high Na content (2.92 wt%) in the edge fuzzy position, which may be due to the mineral being subjected to $Na^+$-containing solution, thus replacing $K^+$ in potassium feldspar. The above cases can be categorized as insoluble forms of AAEMs.

The B2-R observations are shown in Figures 11 and 12, respectively. B2-R exhibits a greater degree of intricate mineral symbiosis than B2-I. As shown in Figure 11, the particles are composed of fusinite and semifusinite, and part of the cell cavity of fusinite is filled with minerals such as kaolinite and calcite, while mineral particles containing AAEMs are detected in one of the cell cavities of fusinite (Figure 11C). The EDS analysis results in Figure 11D reveal that the composition of the elements at Spots 5 and 6 are
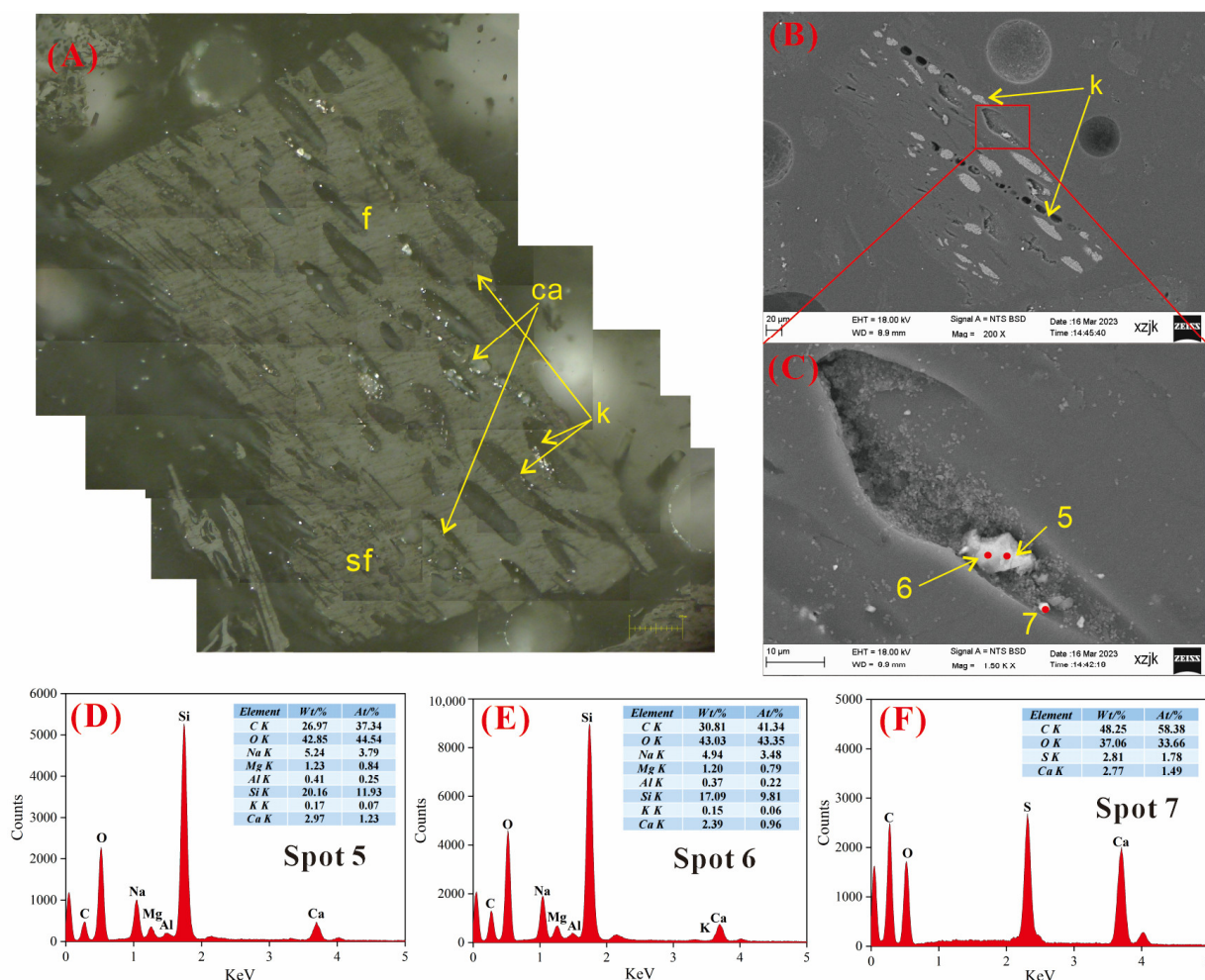
relatively intricate. Compared with other AAEMs, the content of Na was significantly higher (5.24 wt%). Ca (2.97 wt%), Mg (1.23 wt%), and K (0.17 wt%) decreased successively. Quartz ($SiO_2$) is the main mineral at this spot, the atomic ratio of Ca and Mg is close to 1:1, and dolomite ($CaMg(CO_3)_2$) may be mixed into quartz for mineral inclusion. Na enrichment at this point can be attributed to two hypotheses. The first hypothesis suggests that Na is present in carbonate minerals as soluble carbonate ($NaHCO_3$), which falls under the category of water-soluble sodium. Alternatively, the second hypothesis posits the presence of fluid inclusions within quartz itself, primarily resulting from the infiltration of the highly mineralized fluids into the fissures between the formed quartz crystals [47]. Spot 7 represents the scattered calcium sulfate ($CaSO_4 \cdot H_2O$) particles, which are presumably derived from the interaction between $SO_4^{2-}$ and calcite in groundwater [48].



**Figure 10.** Microscope and SEM–EDS identification of B2-I: (**A**) a fusinite (f) particle; (**B**) SEM image of (**A**); (**C**) magnified SEM image of the red boxed area in (**B**); (**D**,**E**) EDS spectra from Spot 3 and 4, respectively.

The phenomenon of mineral association is also shown in Figure 12. Indeed, in Figure 12, AAEM-containing mineral crystals are shown to be found in the cell cavity of a semifusinite particle. According to the elemental composition of Spot 8 (Figure 12D), the main mineral at this spot was $SiO_2$, and Ca and Mg are believed to exist in the form of calcite ($CaCO_3$) and dolomite ($CaMg[CO_3]_2$), respectively. Additionally, Na exists in the form of water-soluble sodium ($NaHCO_3$). The contents of K and Al within $SiO_2$ crystals were very low, as they serve as mechanisms for the charge compensation of impurities. The
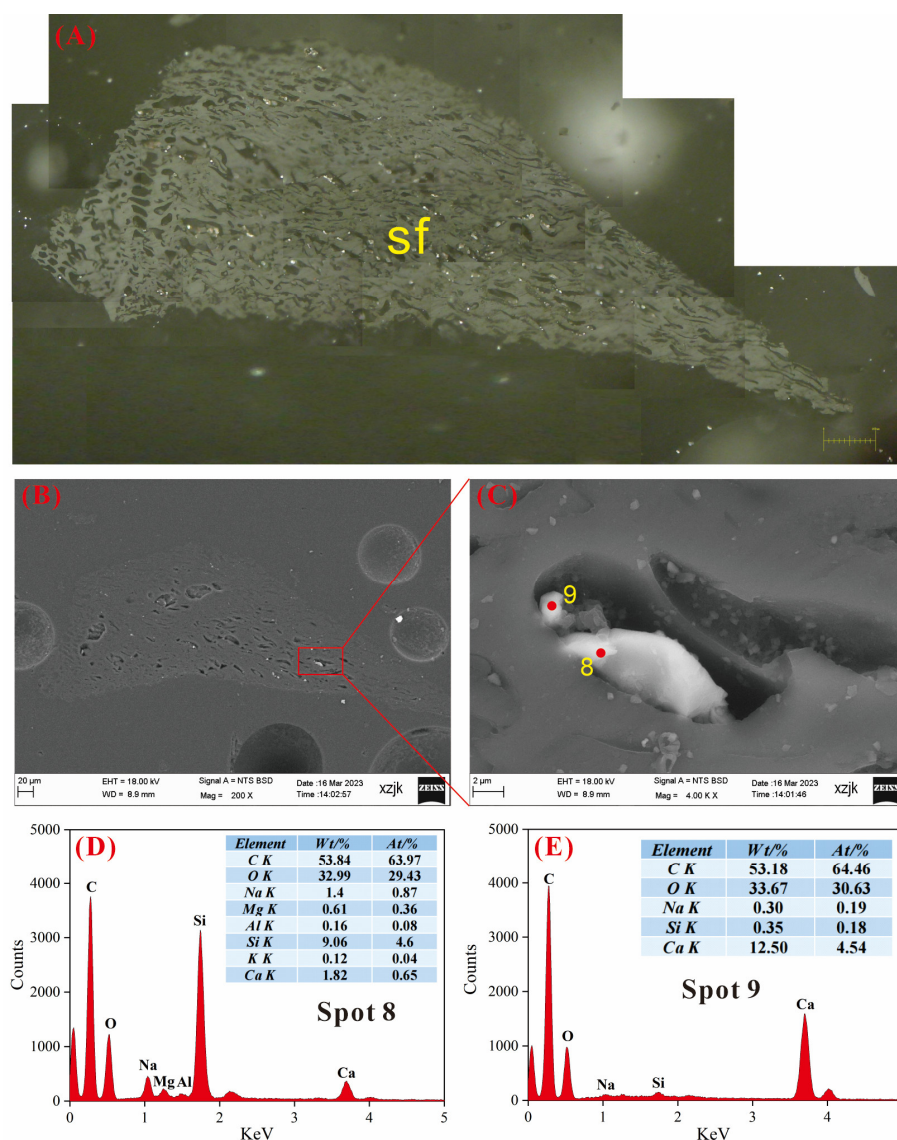
mineral occurrence characteristics at this point reflect the input of multiple hydrothermal fluids or the precipitation of the same fluid at different stages [49]. Quartz, calcite, and dolomite are co-filled in the semifusinite cell cavity, which indicates that quartz originates from the authigenic precipitation of Si fluid while calcite and dolomite mainly originate from the precipitation of $Ca^{2+}$- and $Mg^{2+}$-rich pore solutions [50–52].



**Figure 11.** Microscope and SEM–EDS identification of B2-R: (**A**) a particle exhibits the adjacency of fusinite (f) and semifusinite (sf), and the cells of fusinite (f) filled with calcite (ca) and kaolinite (k); (**B**) SEM image of (**A**); (**C**) magnified SEM image of the red circle area in (**B**); (**D**–**F**) EDS spectra from Spots 5–7, respectively.

The element composition of Spot 9 consists of calcite ($CaCO_3$), which is one of the minerals most commonly associated with quartz. In addition, a small amount of Si may come from scattered quartz particles, and $Na^+$ exists in $CaCO_3$ by forming an isomorphism. Notably, the Na content at Spot 8 is 1.4 wt%, which is significantly higher than that at Spot 9 (0.3 wt%), indicating a greater propensity for Na to exist in the form of soluble sodium salt within quartz minerals.
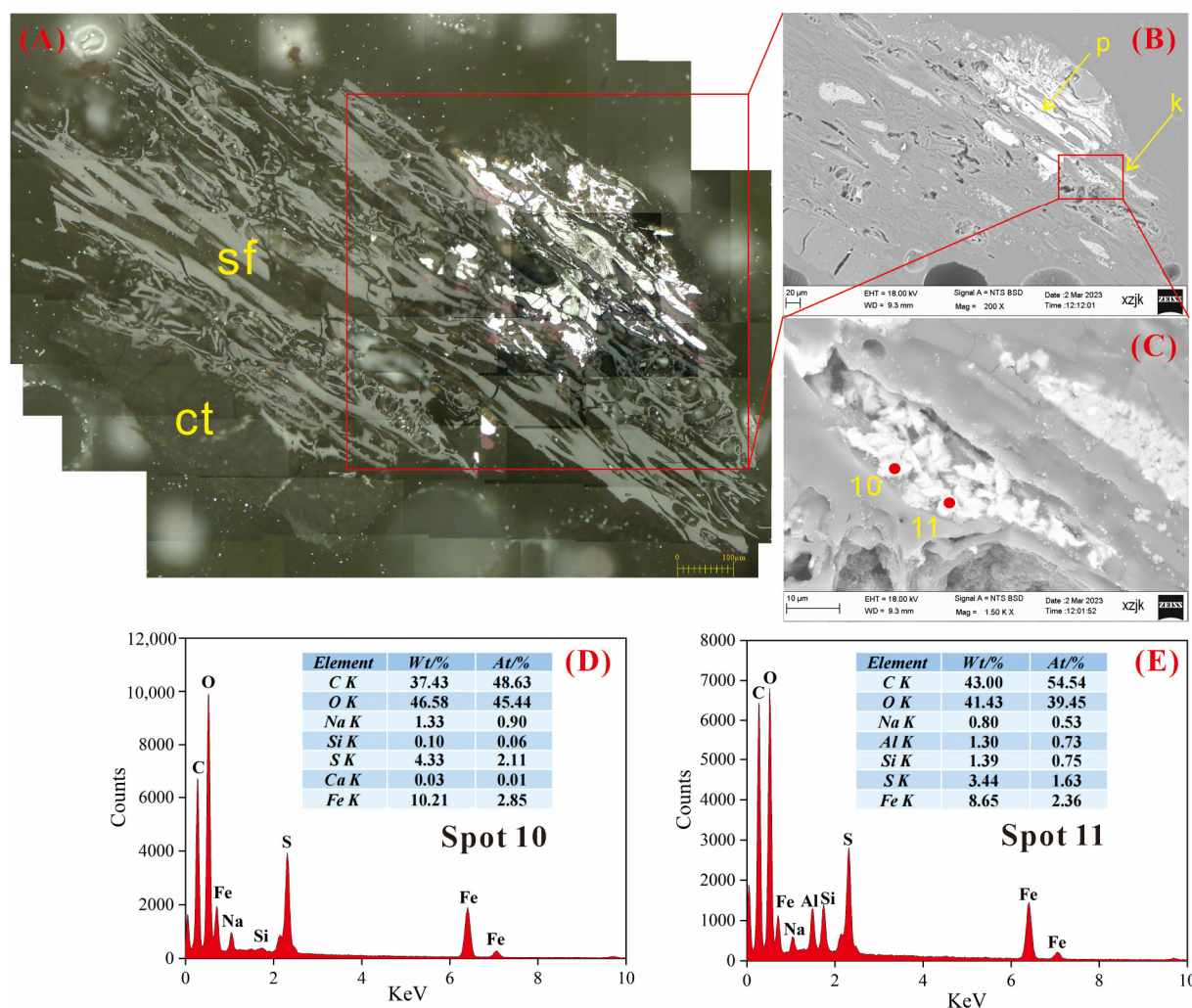
**Figure 12.** Microscope and SEM–EDS identification of B2 raw coal: (**A**) a semifusinite (sf) particle; (**B**) SEM image of (**A**); (**C**) magnified SEM image of the red boxed area in (**B**); (**D**,**E**) EDS spectra from Spots 8 and 9, respectively.

### 4.6.2. AAEMs Occurrence Characteristics of B3-R and B3-V

Minor Na enrichment was detected in the B3-R, which appeared in the pyrite of a semifusinite and collotelinite combined particle. As shown in Figure 13, massive pyrite and kaolinite minerals were filled in the semifusinite cell cavity, while Na enrichment mainly occurred in the massive pyrite filled in the cell cavity. As we can see in the EDS detection results shown in Figure 13D,E, the atomic percentages of Fe at both points were higher than those of the S element. The C/O values (1.23) at the scanning locations were lower than the C/O values (4.53) detected in the ultimate analysis of B3-R, indicating that there is a mineral association between pyrite ($FeS_2$) and siderite ($FeCO_3$) in this region, resulting in high Fe and O contents. Furthermore, small amounts of Al and Si were detected at Spot 11, and the atomic ratio was close to 1:1, indicating that kaolinite ($Al_2Si_2O_5[OH]_4$) existed as the matrix of pyrite at this spot. In addition, the Na contents at the two spots also exhibited a slight disparity. The contents of S, Fe, and Na at Spot 10 were slightly higher than those at Spot 11, indicating that Na mainly exists in pyrite in the form of $Na_2SO_4$. The massive pyrite filled in the semifusinite cell was mainly formed in the late diagenetic stage, and it was formed via the precipitation of sulfur-containing solution penetrating into the coal
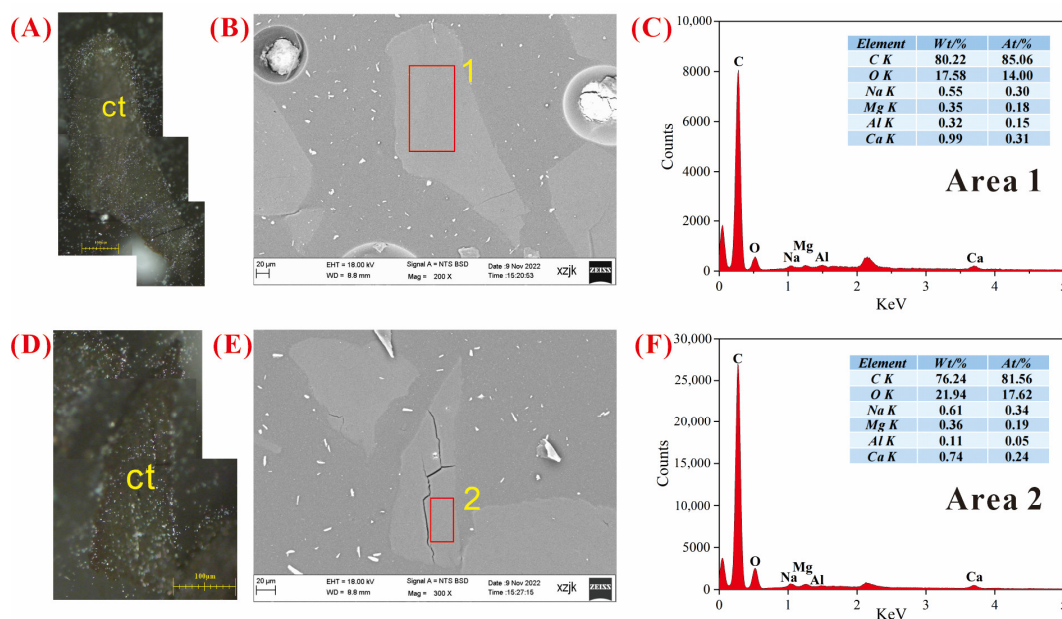
seam [49,53]. $Na^+$ precipitated from albite in coal under the influence of hydrothermal alteration [54], migrated into the cell cavity, and reacted with sulfur-containing solution to form the soluble sodium salt $Na_2SO_4$.



**Figure 13.** Microscopy and SEM-EDS identification of B3-R: (**A**) a particle composed of semifusinite (sf) and collotelinite (ct); (**B**) SEM image of (**A**), where pyrite (p) and kaolinite (k) are symbiotic and filled in the cell cavity; (**C**) magnified SEM image of the area marked red in (**B**); (**D**) and (**E**) are EDS spectra of Spots 10 and 11, respectively.

A significant amount of coal particles consisting of collotelinite were observed in the B3-V, exhibiting distinct outlines, homogeneous composition, and well-developed endogenous fractures. At the same time, we found it challenging to identify any discernible features of inorganic Na and Ca. Figure 14 shows the typical collotelinite observed in B3-V. Regional EDS scanning was conducted on the uniformly distributed collotelinite surface. The results are depicted in Figure 14C,F, with C and O constituting the principal components and containing traces of Na, Mg, Al, and Ca. We speculate that the occurrence of Na and Ca in the two regions was combined with organic matter, as shown in sequential extraction data, to constitute Na/Ca-NH$_4$Cl and Na/Ca-EDTA. The observation results of SEM-EDS were also consistent with the result stating that Na/Ca-NH$_4$Cl and Na/Ca-EDTA occupy more space in B3-V in sequential extraction.

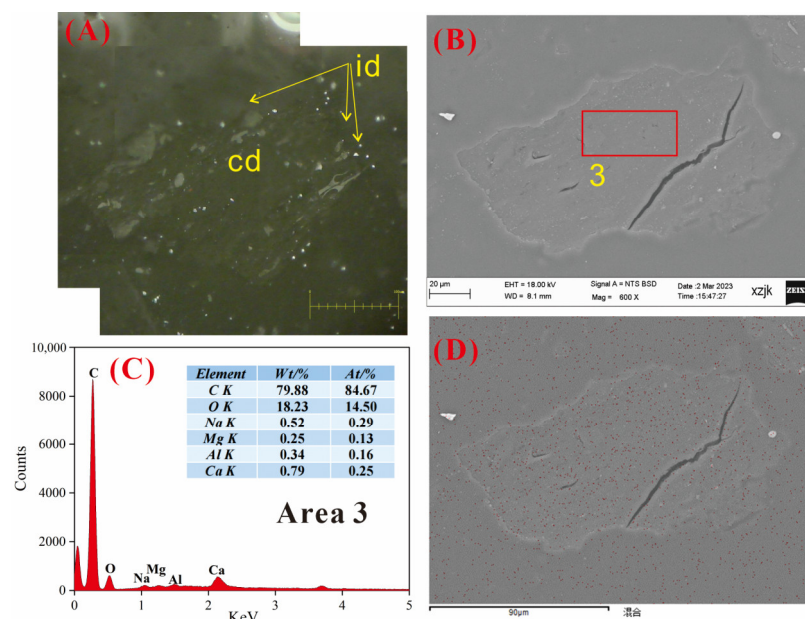**Figure 14.** Microscopy and SEM-EDS identification of B3-V: (**A,D**) a particle of collotelinite (ct); (**B**) SEM image of (**A**); (**C**) EDS spectra of the area marked red in (**B**); (**E**) SEM image of (**D**); (**F**) EDS spectra of the area marked red in (**E**).
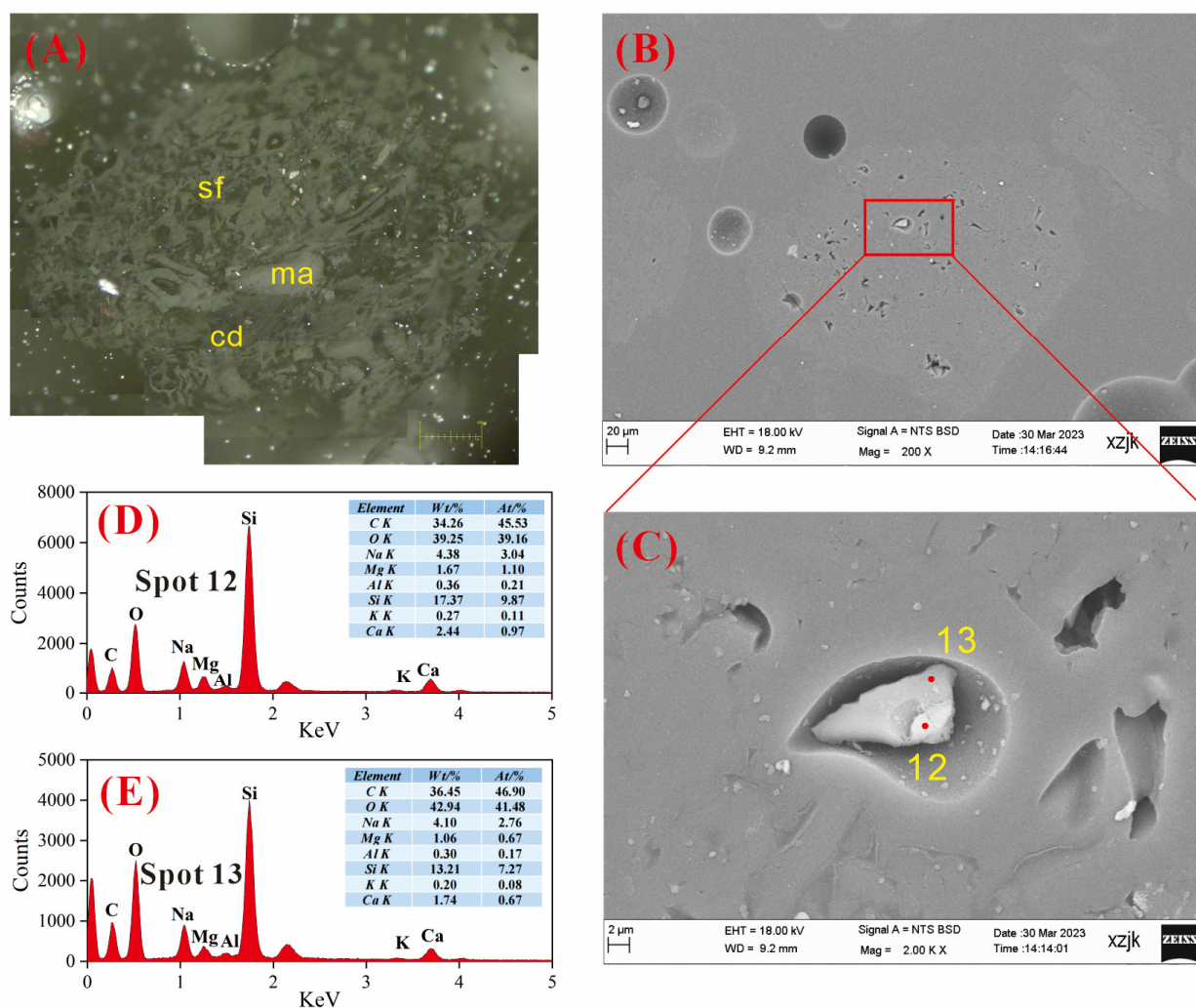
### 4.6.3. AAEMs Occurrence Characteristics of B5-R, B5-I, and B5-V

B5-V showed similar maceral characteristics to those of B3-V. Figure 15 shows a collodetrinite particle found in the B5-V with some idertodetrinites scattered on its surface. Area scanning was performed on the uniform position on the surface of the collodetrinite, and the results are shown in Figure 15C. The EDS spectra results were very similar to those of B3-V; thus, we also believe that Na and Ca were mainly combined with organic matter. Figure 15D shows the mixed image of Na after scanning via mapping. We can see that Na is uniformly distributed and dispersed on the surface of organic matter without local enrichment.



**Figure 15.** Microscopy and SEM-EDS identification of B5-V: (**A**) a collodetrinite (cd) particle on the surface with some idertodetrinites (id); (**B**) SEM image of (**A**); (**C**) EDS spectra of the area marked red in (**B**); (**D**) Na EDS mapping of (**B**).
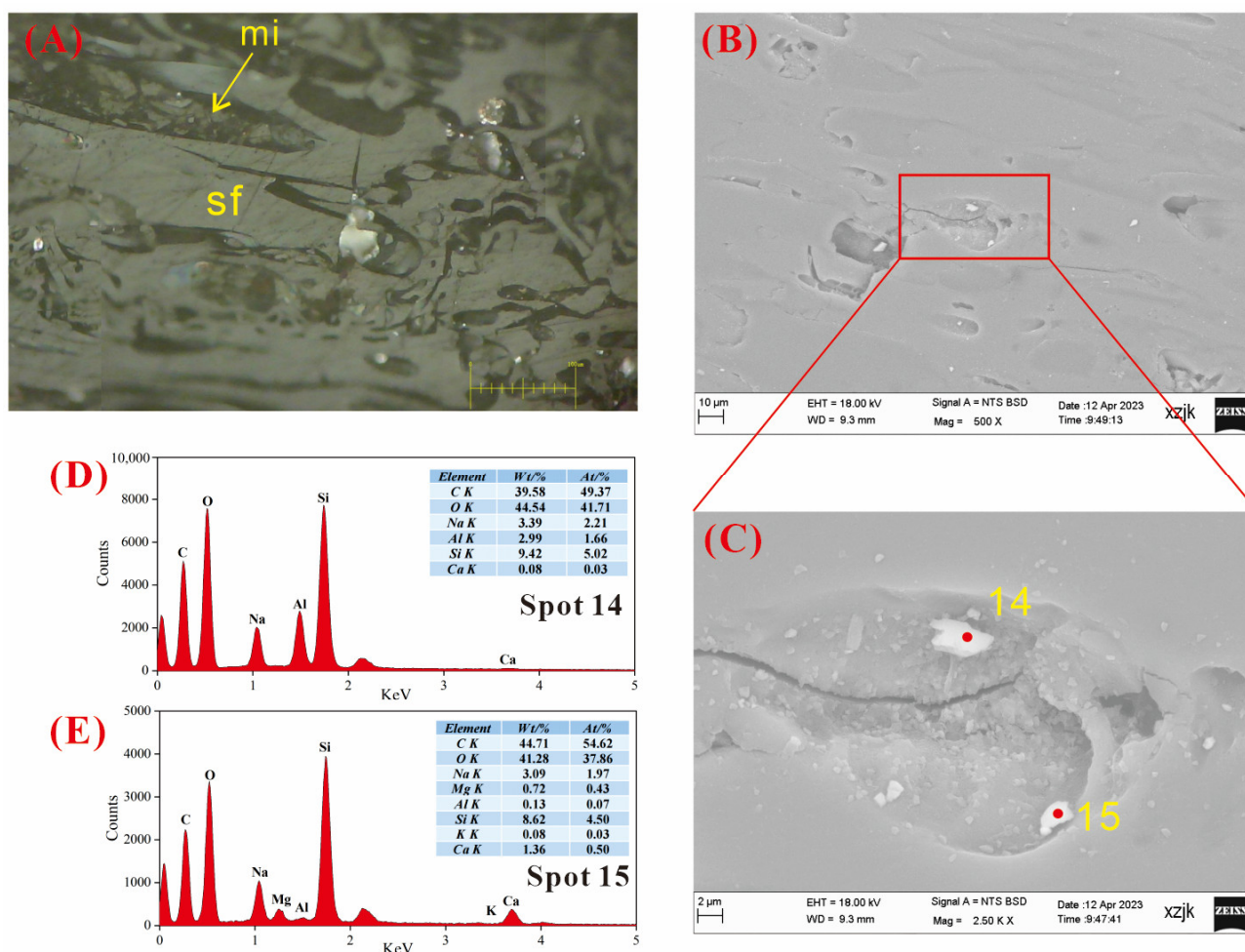
B5-R has the highest amounts of AAEMs among the raw coal samples, and the AAEM particles found in this sample generally have high contents (Figures 16 and 17). As shown in Figure 16, AAEM-containing crystals were found in the semifusinite cell cavity of the particles composed of semifusinite, collodetrinite, and macrinite. Two spots on the crystal surface were selected for EDS analysis, and the results are shown in Figure 16D. The main minerals were quartz ($SiO_2$) and dolomite ($CaMg[CO_3]_2$), which existed as associated minerals. Na existed in the form of soluble sodium salt ($NaHCO_3$), and small amounts of Al and K elements were mixed into the quartz crystal in the form of isomorphism.



**Figure 16.** Microscopy and SEM-EDS identification of B5-R: (**A**) a particle composed of semifusinite (sf), collodetrinite (cd), and macrinite (ma); (**B**) SEM image of (**A**); (**C**) magnified SEM image of the area marked red in (**B**); (**D,E**) EDS spectra of Spots 12 and 13, respectively.

As shown in Figure 17, two AAEMs-containing minerals with different element compositions were filled in the semifusinite cell cavity, indicating that they were both symbiotic minerals. Spot 14 is a plate-like crystal, and the EDS spectra show a slight Na enrichment (3.39 wt%). In addition to C and O, the atomic percentages of each element at this point were 2.21at% for Na, 1.66at% for Al, 5.02at% for Si, and 0.03at% for Ca, and the main mineral at this point was albite ($NaAlSi_3O_8$). Moreover, the high atomic percentage of Na relative to the Al suggests that some $NaHCO_3$ may accompany this point. Spot 15 is a massive crystal, and the EDS spectra also show the enrichment of Na (3.09 wt%) and Ca (1.36 wt%), and it is evident that the point is mainly quartz ($SiO_2$), associated with dolomite ($CaMg[CO_3]_2$) minerals, while Na exists in the form of $NaHCO_3$.

**Figure 17.** Microscopy and SEM-EDS identification of B5-R: (**A**) a particle composed of semifusinite (sf) and micrinite (mi); (**B**) SEM image of (**A**); (**C**) magnified SEM image of the area marked red in (**B**); (**D**,**E**) EDS spectra of Spots 14 and 15, respectively.
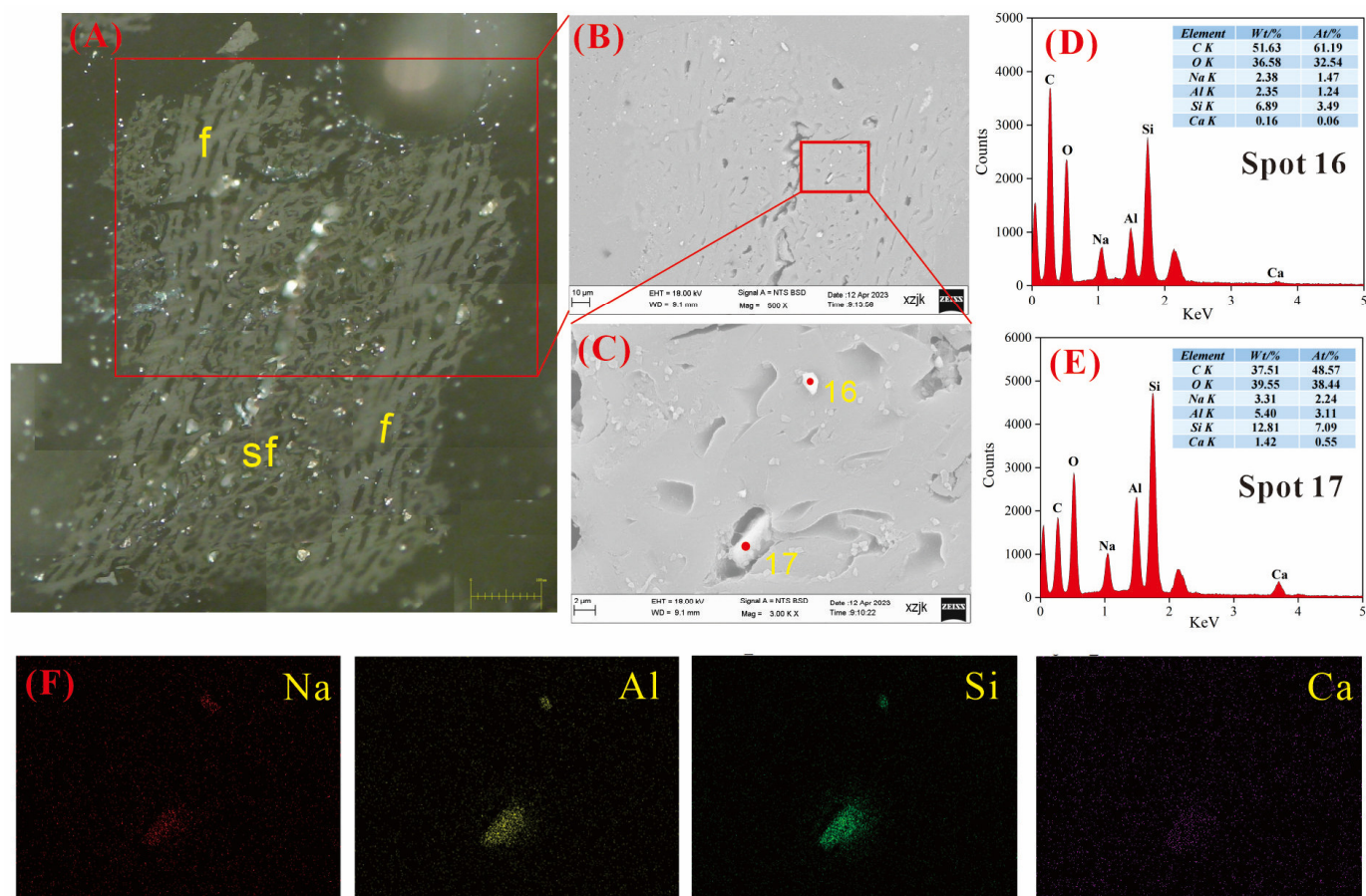
Figures 18 and 19 are AAEM-containing particles found in B5-I. As shown in Figure 18, AAEM-containing crystals were found both in the cell cavity of semifusinite and on the surface of the organic matter. The local enrichment of Na is shown in the face-scanning results of Figure 18F, in contrast to the local enrichment of Ca, which is not obvious and primarily uniformly distributed on the coal matrix. We can surmise that most Ca is uniformly combined with organic matter as both Ca-$NH_4$Cl and Ca-EDTA. According to the EDS spectra results at Spots 16 and 17, the Na enrichment content reached 2.38 wt% and 3.31 wt%, respectively. Moreover, according to the atomic percentage analysis, the main mineral compositions at these spots were albite ($NaAlSi_3O_8$) and plagioclase ($Na[AlSi_3O_8]$-$Ca[Al_2Si_2O_8]$), respectively.

Of these elements, Na's atomic percentage is higher than that of Al in the albite mineral at Spot 16. Since Na is distributed on the surface of organic matter and EDS scanning has a certain depth, we assumed that the additional Na was combined with organic matter and evenly distributed in the coal matrix. Notably, the albite at Spot 16 is semi-autogenous and distributed on the surface of the organic matter, and this mineral is mainly of terrigenous clastic origin. In contrast, the plagioclase particles at Spot 16 are quadrilateral granules filled with inertinite constituent cells, indicating that they are authigenic causal minerals, formed via the precipitation of $Na^+$- and $Ca^{2+}$- rich groundwater fluids in the cell cavity [55].

Figure 19 shows the region with the highest Na content (5.85 wt%) in this survey. This particle is mainly composed of semifusinite and fusinite, in which kaolinite minerals are filled in the cell cavity of fusinite in the form of pisiform aggregate, and AAEM-containing
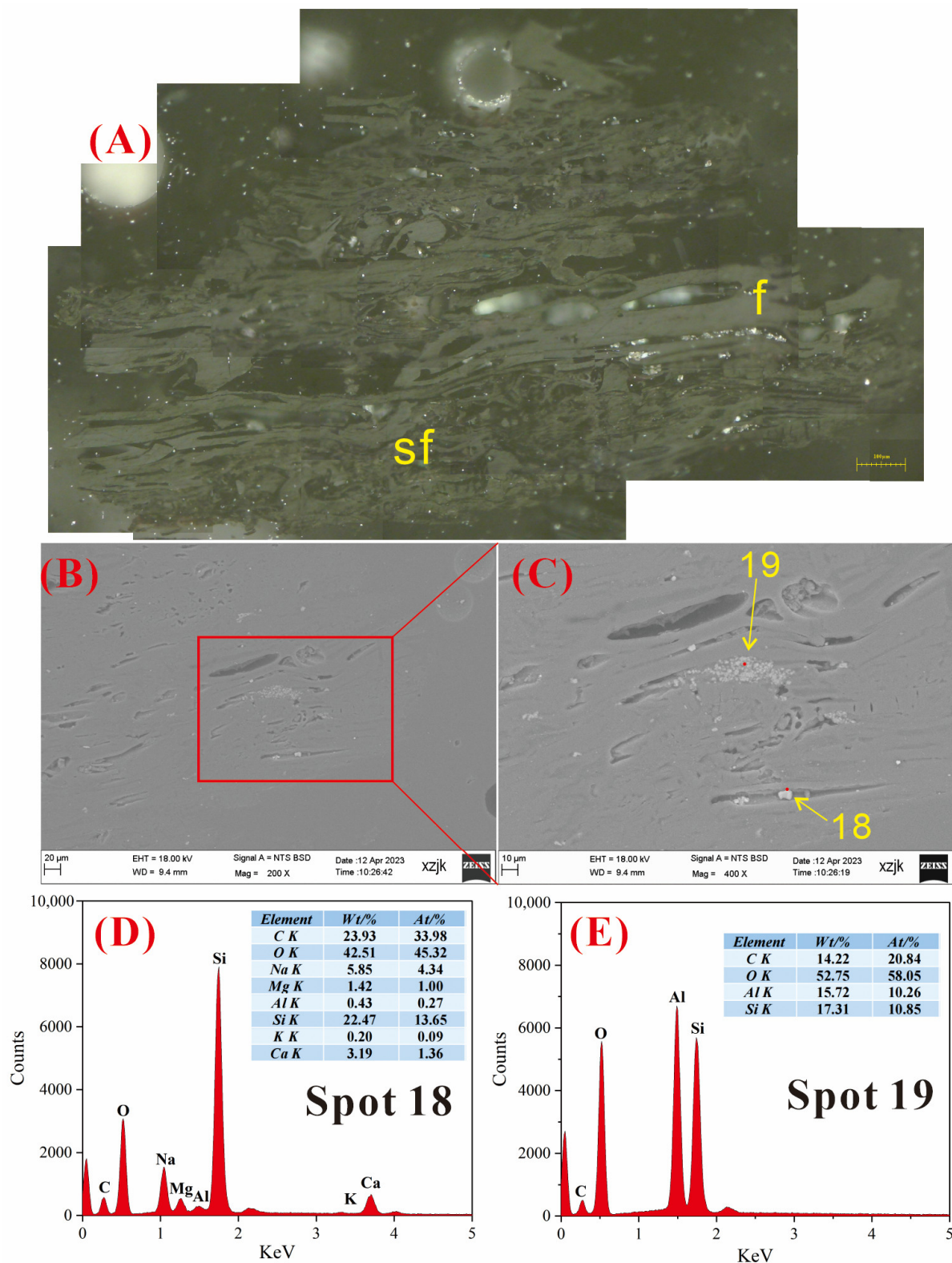
crystals are filled in the cell cavity below it in a semi-autogenous structure, both being autogenous minerals. According to the EDS spectra of Spot 18, the main minerals at this point are quartz ($SiO_2$); Ca and Mg, which exist in the form of dolomite minerals ($CaMg[CO_3]_2$); and Na, which exists in the form of $NaHCO_3$ in quartz crystals. The enrichment of AAEMs at this spot may also originate from the action of alkaline fluids.



**Figure 18.** Microscopy and SEM-EDS identification of B5-I: (**A**) a particle composed of fusinite (f) and semifusinite (sf); (**B**) SEM image of (**A**); (**C**) magnified SEM image of the area marked red in (**B**); (**D**,**E**) EDS spectra of Spots 15 and 16, respectively; (**F**) Na, Al, Si, and Ca EDS mapping of (**C**).

*4.7. Differences between the Occurrence of AAEMs in Maceral Groups*

By analyzing the observations obtained via combined optical microscopy and SEM-EDS, we found that most inorganic Na was distributed in the inertinite cell cavity, with water-soluble Na (Na-Water) in the form of $NaHCO_3$ accounting for the majority of this content, most of which is present in quartz minerals (average content: 4.14 wt%), though a small portion is present with pyrite (average content: 1.07 wt%). The carrier minerals of insoluble Na (Na-I) are dominated by alkali feldspar minerals (average content: 2.62 wt%), though they are present to a lesser extent in the form of clay minerals (0.9 wt%). In addition, a small amount of Na is present with the carbonate minerals, and this part belongs to Na-HCl. Nevertheless, no local enrichment of Na was detected in the vitrinite-enriched sample (B3-V, B5-V), where Na was uniformly bound to the organic matter and distributed on the surface, and the Na content was lower than those of the raw coal and inertinite-enriched samples. In summary, Na in Xiheishan coal is more widely distributed in the inertinite group, with a higher content and various occurrence modes.

**Figure 19.** Microscopy and SEM-EDS identification of B5-I: (**A**) a particle composed of semifusinite (sf) and fusinite (f); (**B**) SEM image of (**A**); (**C**) magnified SEM image of the area marked red in (**B**); (**D**,**E**) EDS spectra of Spots 18 and 19, respectively.

The results of the sequential extraction method show that most of the Ca and Mg present in the samples were in organic form. Nonetheless, the organic structure could not be directly observed via SEM-EDS, meaning that the correlation of Ca and Mg with the

maceral groups could not be directly analyzed. However, during SEM-EDS observation, dolomite and calcite minerals associated with quartz were identified several times in the inertinite cell cavity, which belongs to acid-soluble carbonate (Ca/Mg-HCl). Nevertheless, only small amounts of Ca and Mg were uniformly distributed on the surface of the organic matter in the inertinite-enriched samples. Therefore, our results indirectly indicate that Ca and Mg in Xiheishan coal tend to be enriched in the inertinite group.

K in the Xiheishan coal mainly exists in the form of insoluble K (K-I), and its content is very low, meaning that it is difficult to judge its correlation with maceral groups.

Based on the above maceral identification method, AAEM content test, sequential extraction results, and SEM-EDS analysis of raw coal samples and maceral enrichment samples extracted from the Xiheishan Mine, it is evident that AAEMs in coal samples have a closer relationship with the inertinite group. In addition, inertinite is richer in minerals, meaning that, in the subsequent removal of AAEMs from Xiheishan coal via pre-treatment, quartz and other minerals can be studied, and gravity separation can be considered part of the AAEMs removal process.

## 5. Conclusions

Based on the sequential extraction experiments, inductively coupled plasma–atomic emission spectroscopy (ICP-AES), optical microscopy, SEM-EDS, and the use of an ion chromatograph, the differences between the occurrence of AAEMs in different macerals and the correlation between the two types in the coal from the Zhundong Xiheishan mining area were discussed. The results are as follows:

(1) The coal of the Xishanyao Formation in the Zhundong Xiheishan mining area has the characteristics of medium–high moisture, extremely low ash, medium–high volatility, and low sulfur. In the raw coal samples (B2-R, B3-R, B5-R), all the critical metal elements except for Sr are at deficit levels.

(2) The AAEMs in the samples are dominated by Ca, Na, and Mg, and the contents of Na, Ca, and Mg showed a trend of increasing in line with the increase in the inertinite content. The total amount of AAEMs in the inertinite-enriched samples was significantly higher than the amounts in the rest of the samples, ranked in the following order: B5-I > B2-I > B2-R> B5-R > B3-R > B5-I > B3-I.

(3) The sequential extraction results showed that occurrence mode patterns for Na in the raw coal samples and the inertinite-enriched samples were similar, with Na mainly being dominated by Na-Water, followed by organic sodium, including Na-$NH_4$Cl and Na-EDTA, whereas Na in the vitrinite-enriched samples was dominated by organic sodium, of which Na-$NH_4$Cl accounted for most of the samples, followed by Na-Water. The Na-Water in the sample mainly existed in the form of $NaHCO_3$ and $Na_2SO_4$. Ca-EDTA is the main occurrence mode of Ca in all the samples, and the CA-EDTA contents in the vitrinite-enriched samples were higher than those in the other samples. Mg mainly existed in the form of Mg-$NH_4$Cl and Mg-EDTA, which also occupied a relatively high proportion of the vitrinite-enriched samples. The main occurrence mode of K was K-I.

(4) Under SEM-EDS observation, the localized enrichment of AAEMs was identified in raw coal samples and inertinite-enriched samples, with most of these examples found in the inertinite cell cavities. The highest localized enrichment of AAEMs was found in quartz crystals, where Na mainly existed in the form of $NaHCO_3$ (Na-Water) (up to 5.85 wt%), and Ca and Mg accompanied it as dolomite and calcite minerals. Also, alkali feldspar minerals were found several times in the inertinite group. However, no localized enrichment of any AAEMs were found in the vitrinite-enriched samples. In summary, AAEMs were more inclined to be enriched in the inertinite group, likely due to the structural characteristics of having abundant pores.

## References

1. Zhou, J.; Zhuang, X.; Alastuey, A.; Querol, X.; Li, J.H. Geochemistry and mineralogy of coal in the recently explored Zhundong large coal field in the Junggar basin, Xinjiang province, China. *Int. J. Coal Geol.* **2010**, *82*, 51–67. [CrossRef]
2. Zhang, Y.; Zhang, H.; Zhu, Z. Physical and chemical properties of fly ash from fluidized bed gasification of Zhundong coal. *Fuel Chem. Technol.* **2016**, *44*, 305–313. (In Chinese)
3. Li, J.; Zhuang, X.; Querol, X.; Font, O.; Moreno, N.; Zhou, J.B.; Lei, G.M. High quality of Jurassic Coals in the Southern and Eastern Junggar Coalfields, Xinjiang, NW China: Geochemical and mineralogical characteristics. *Int. J. Coal Geol.* **2012**, *99*, 1–15. [CrossRef]
4. Zhu, C.; Qu, S.; Zhang, J.; Wang, Y.; Zhang, Y.H. Distribution, occurrence and leaching dynamic behavior of sodium in Zhundong coal. *Fuel* **2017**, *190*, 189–197. [CrossRef]
5. Li, G.D.; Li, S.Q.; Huang, Q.; Yao, Q. Fine particulate formation and ash deposition during pulverized coal combustion of high-sodium lignite in a down-fired furnace. *Fuel* **2015**, *143*, 430–437. [CrossRef]
6. Wang, X.B.; Xu, Z.X.; Wei, B.; Zhang, L.; Tan, H.Z.; Yang, T.; Mikulcic, H.; Duic, N. The ash deposition mechanism in boilers burning Zhundong coal with high contents of sodium and calcium: A study from ash evaporating to condensing. *Appl. Therm. Eng.* **2015**, *80*, 150–159. [CrossRef]
7. Yang, C.W.; Ding, H.; Bai, X.F.; Tang, Y.G.; He, J.; Yuan, D.Y. Research status of sodium geochemistry in high-sodium Coal in Xinjiang. *Coal Sci. Technol.* **2022**, *50*, 169–178. (In Chinese)
8. Weng, Q.S.; Wang, C.A.; Che, D.F.; Fu, Z.W. Alkali metal occurrence mode and its influence on combustion characteristics in Zhundong coals. *J. Combust. Sci. Technol.* **2014**, *20*, 216–221. (In Chinese)
9. Blaesing, M.; Mueller, M. Release of alkali metal, sulphur, and chlorine species from high temperature gasification of high-and low-rank coals. *Fuel Process. Technol.* **2013**, *106*, 289–294. [CrossRef]
10. Song, G.L.; Yang, S.B.; Song, W.J.; Qi, X.B. Release and transformation behaviors of sodium during combustion of high alkali residual carbon. *Appl. Eng.* **2017**, *122*, 285–296. [CrossRef]
11. Zhang, J.; Li, J.; Mao, Y.; Bi, J.C.; Zhu, M.M.; Zhang, Z.Z.; Zhang, L.; Zhang, D.K. Effect of $CaCO_3$ addition on ash sintering behaviour during $K_2CO_3$ catalysed steam gasification of a Chinese lignite. *Appl. Therm. Eng.* **2017**, *111*, 503–509. [CrossRef]
12. Zhang, Z.; Pang, S.; Levi, T. Influence of AAEM species in coal and biomass on steam co-gasification of chars of blended coal and biomass. *Renew. Energy* **2017**, *101*, 356–363. [CrossRef]
13. Chen, C.; Zhang, S.Y.; Liu, D.H.; Guo, X.; Dong, A.X.; Xiong, Z.W.; Shi, D.Z.; Lv, J.F. Existence form of sodium in high sodium coals from Xinjiang and its effect on combustion process. *J. Fuel Chem. Technol.* **2013**, *41*, 832–838.
14. Wu, L.; Qiao, Y.; Gui, B.; Wang, C.; Xu, J.Y.; Yao, H.; Xu, M.H. Effects of chemical forms of alkali and alkaline earth metallic species on the char ignition temperature of a loy yang coal under $O_2/N_2$ atmosphere. *Energy Fuels* **2012**, *26*, 112–117. [CrossRef]
15. Li, R.; Chen, Q.; Zhang, H. Detailed investigation on sodium (Na) species release and transformation mechanism during pyrolysis and char gasification of high-Na Zhundong coal. *Energy Fuels* **2017**, *31*, 5902–5912. [CrossRef]
16. Xie, K.C. *Structure and Reactivity of Coal*; Science Press: Beijing, China, 2002.
17. Zhao, Y.; Hu, H.; Jin, L.; He, X.F.; Wu, B. Pyrolysis behavior of vitrinite and inertinite from Chinese Pingshuo coal by TG–MS and in a fixed bed reactor. *Fuel Process. Technol.* **2011**, *92*, 780–786. [CrossRef]
18. brodzki, D.; Akar, A. Comparison by gc-ms of liquefaction extracts from coal maceral concentrates. *Fuel* **1995**, *36*, 407–415. [CrossRef]
19. Guo, H.N.; Shi, H.; Wu, Y.X.; Lyu, J.F.; Zhang, Y. Mineral transformation during rapid heating and cooling of Zhundong coal ash. *Fuel* **2022**, *310*, 122269. [CrossRef]

20. Zhang, D.L.; Zhou, J.B.; Zhuang, X.G.; Lei, D.M.; Song, Z.H. Xishanyao Formation Coal Facies Characteristics in Xiheishan Exploration Area, Eastern Junggar Coalfield, Xinjiang. *Coal Geol. China* **2014**, *26*, 1–7. (In Chinese)

21. He, X.; Wang, W.F.; Yang, Y.T.; Zhou, C.C.; He, J.F.; Duan, P.P.; Lu, Q.F. Occurrence Relationship between Sodium and Maceral Groups in Subbituminous Coal: A Case Study on Zhundong Cola and Shenfu Coal. *Minerals* **2023**, *13*, 122. [CrossRef]

22. He, X.; Sun, H.; Chen, X.W.; Zhao, B.; Zhang, X.X.; Komarneni, S. Charging mechanism analysis of macerals during triboelectrostatic enrichment process: Insights from relative dielectric constant, specific resistivity and X-ray diffraction. *Fuel* **2018**, *225*, 533–541. [CrossRef]

23. He, X.; Sun, H.; Zhao, B.; Chen, X.W.; Zhang, X.X.; Komarneni, S. Tribocharging of macerals with various materials: Role of surface oxygen-containing groups and potential difference of macerals. *Fuel* **2018**, *233*, 750–768. [CrossRef]

24. Chen, X.W.; Zhuang, X.G.; Zhou, J.B.; Zeng, X.J.; A, M.N.; Ge, D.F.; Yang, S. Coal quality and its distribution of the eastern Junggar coalfield in Junggar basin, Xinjiang. *Xinjiang Geol.* **2013**, *31*, 89–93.

25. Benson, S.A.; Holm, P.L. Comparison of inorganics in three low-rank coals. *Ind. Eng. Chem. Prod. Res. Dev.* **1985**, *24*, 145–149. [CrossRef]

26. Finkelman, R.B.; Palmer, C.A.; Wang, P. Quantification of the modes of occurrence of 42 elements in coal. *Int. J. Coal Geol.* **2018**, *185*, 138–160. [CrossRef]

27. Matsuoka, K.; Rosyadi, E.; Tomita, A. Mode of occurrence of calcium in various coals. *Fuel* **2002**, *81*, 1433–1438. [CrossRef]

28. He, X.; Che, K.; Pan, J.; Sun, H.; Zhou, C.C.; Wang, W.F. Occurrence Mode of Sodium in Zhundong Coal, China: Relationship to Maceral Groups. *Minerals* **2023**, *13*, 1155. [CrossRef]

29. Grigore, M.; Sakurovs, R. Inorganic matter in Victorian brown coals. *Int. J. Coal Geol.* **2016**, *154*, 257–264. [CrossRef]

30. *GB/T 212-2008*; Proximate analysis of coal. China Coal Industry Association: Beijing, China, 2008.

31. *GB/T 214-2007*; Determination of total sulfur in coal. China Coal Industry Association: Beijing, China,, 2007.

32. *GB/T 19227-2008*; Determination of nitrogen in coal. China Coal Industry Association: Beijing, China, 2008.

33. *GB/T 476-2008*; Determination of carbon and hydrogen in coal. China Coal Industry Association: Beijing, China, 2008.

34. ICCP. The new vitrinite classification (ICCP System 1994). *Fuel* **1998**, *77*, 349–358. [CrossRef]

35. ICCP. The new inertinite classification (ICCP System 1994). *Fuel* **2001**, *80*, 459–471. [CrossRef]

36. Pickel, W.; Kus, J.; Flores, D. Classification of liptinite-ICCP System 1994. *Int. J. Coal Geol.* **2017**, *169*, 40–61. [CrossRef]

37. Sykorova, I.; Pickel, W.; Christanis, K.; Wolf, M.; Taylor, G.H.; Flores, D. Classification of huminite-ICCP System 1994. *Int. J. Coal Geol.* **2005**, *62*, 85–106. [CrossRef]

38. *GB/T 6948-2008*; Method of determining microscopically the reflectance of vitrinite in coal. China Coal Industry Association: Beijing, China, 2008.

39. He, X.; Sun, H.; Ma, M.Y.; Zhang, X.X.; Wang, W.F. Enrichment Characteristics of Macerals during Triboelectrostatic Separation in the View of Surface Microstructure, Pore distribution, and Typical Electrical Parameters. *ACS Omega* **2021**, *6*, 18509–18517. [CrossRef] [PubMed]

40. He, X.; Zhang, X.X.; Jiao, Y.; Zhu, J.S.; Chen, X.W.; Li, C.Y.; Li, H.S. Complementary analyses of infrared transmission and diffuse reflection spectra of macerals in low-rank coal and application in triboelectrostatic enrichment of active maceral. *Fuel* **2017**, *192*, 93–101. [CrossRef]

41. Weck, P.F.; Kim, E.; Wang, Y.; Kruichak, J.N.; Mills, M.M.; Matteo, E.N.; Pellenq, R.J.M. Model representations of kerogen structures: An insight from density functional theory calculations and spectroscopic measurements. *Sci. Rep.* **2017**, *7*, 7068. [CrossRef] [PubMed]

42. Yao, Z.; Luo, Q.Z.; Li, N.; Li, H.B.; Wang, Q.; Gao, J. Occurrence characteristics of Carboniferous-Permian tar-rich coal and its influencing factors in Northern Shanxi. *Coal Geol. Explor.* **2021**, *49*, 50–61. (In Chinese)

43. Dai, S.F.; Ren, D.Y.; Chou, C.L.; Finkelman, R.B.; Seredin, V.V.; Zhou, Y.P. Geochemistry of trace elements in chinese coals: A review of abundances, genetic types, impacts on human health, and industrial utilization. *Int. J. Coal Geol.* **2012**, *94*, 3–21. [CrossRef]

44. Yuan, D.Y.; Ding, H.; He, J.; Bai, X.F.; Zhang, Y.H. Influence of surface saline-alkali soil on element characteristics of shallow coal seams in Xishanyao Formation. *Coal Qual. Technol.* **2023**, *38*, 48–55. (In Chinese)

45. Bai, X.F.; Wang, Y.; Ding, H.; Zhu, C.; Zhang, Y.H. Occurrence state of sodium in coal of Zhundong. *J. China Coal Sci.* **2015**, *40*, 2909–2915. (In Chinese)

46. He, X.; Wang, W.F.; Zhang, X.X.; Yang, Y.T.; Sun, H. Distribution characteristics and differences of oxygen-containing functional groups in macerals of low rank coal. *J. China Coal Soc.* **2021**, *46*, 2804–2812.

47. Haus, R.; Prinz, S.; Priess, C. *Quartz: Deposits, Mineralogy and Analytics*; Springer: Berlin/Heidelberg, Germany, 2012; pp. 29–67.

48. Dai, S.F.; Zhang, W.G.; Ward, C.R.; Seredin, V.V.; Hower, J.C.; Li, X.; Song, W.J.; Wang, X.B.; Kang, H.; Zheng, L.C.; et al. Mineralogical and geochemical anomalies of Late Permian coals from the Fusui Coalfield, Guangxi province, southern China: Influences of terrigenous materials and hydrothermal fluids. *Int. J. Coal Geol.* **2013**, *105*, 60–84. [CrossRef]

49. Ward, C.R. Analysis, origin and significance of mineral matter in coal: Anupdated review. *Int. J. Coal Geol.* **2016**, *165*, 1–27. [CrossRef]

50. Lu, Q.F.; Qin, S.J.; Wang, W.F.; Wu, S.H.; Shao, F.J. Mineralogy and Geochemistry of High-Sulfur Coals from the M8 Coal Seam, Shihao Mine, Songzao Coalfield, Chongqing, Southwestern China. *Minerals* **2024**, *14*, 95. [CrossRef]

51. Dai, S.; Li, T.; Seredin, V.V.; Ward, C.R.; Hower, J.C.; Zhou, Y.P.; Zhang, M.Q.; Song, X.L.; Song, W.J.; Zhao, C.L. Origin of minerals and elements in the Late Permian coals, tonsteins, and host rocks of the Xinde Mine, Xuanwei, eastern Yunnan, China. *Int. J. Coal Geol.* **2014**, *121*, 53–78. [CrossRef]
52. Ward, C.R. Analysis and significance of mineral matter in coal seams. *Int. J. Coal Geol.* **2002**, *50*, 135–168. [CrossRef]
53. Liu, D.M.; Yang, Q.; Zhou, C.; Tang, D.Z.; Kang, X.D. Occurrence character istics and ge-ological genesis of pyrite in late Paleozoic coal in North China. *Geochimica* **1999**, *28*, 340–350. (In Chinese)
54. Yu, L.D.; Sun, H.W.; Zhang, J.; He, X.H.; Xue, D.; Dan, W.; Sun, Y.Q. Hydrothermal alteration and element migration in the Yufeng gold deposit, Eastern Tianshan Orogen. *Acta Petrol. Sin.* **2020**, *36*, 14. (In Chinese)
55. Zhao, L.; Ward, C.R.; French, D.; Graham, I.T. Mineralogy of the volcanic-influenced Great Northern coal seam in the Sydney Basin, Australia. *Int. J. Coal Geol.* **2012**, *94*, 94–110. [CrossRef]